

Kinetic temperature of massive star-forming molecular clumps measured with formaldehyde

V. The massive filament DR21

X. Zhao^{1,2}, X. D. Tang^{1,2,3,4}, C. Henkel^{5,1}, Y. Gong^{5,6}, Y. Lin^{5,7}, D. L. Li^{1,2,3,4}, Y. X. He^{1,2,3,4}, Y. P. Ao⁶, X. Lu⁸, T. Liu⁸, Y. Sun⁶, K. Wang⁹, X. P. Chen⁶, J. Esimbek^{1,3,4}, J. J. Zhou^{1,3,4}, J. W. Wu^{10,2}, J. J. Qiu¹¹, X. W. Zheng¹², J. S. Li^{1,2}, C. S. Luo^{1,2}, and Q. Zhao^{1,2}

¹ Xinjiang Astronomical Observatory, Chinese Academy of Sciences, 830011 Urumqi, PR China
e-mail: tangxindi@xao.ac.cn

² University of Chinese Academy of Sciences, 100080 Beijing, PR China

³ Key Laboratory of Radio Astronomy, Chinese Academy of Sciences, 830011 Urumqi, PR China

⁴ Xinjiang Key Laboratory of Radio Astrophysics, Urumqi 830011, PR China

⁵ Max-Planck-Institut für Radioastronomie, Auf dem Hügel 69, 53121 Bonn, Germany

⁶ Purple Mountain Observatory, Chinese Academy of Sciences, Nanjing 210008, PR China

⁷ Max-Planck-Institut für Extraterrestrische Physik, Giessenbachstr. 1, 85748 Garching bei München, Germany

⁸ Shanghai Astronomical Observatory, Chinese Academy of Sciences, 80 Nandan Road, Shanghai 200030, PR China

⁹ Kavli Institute for Astronomy and Astrophysics, Peking University, Beijing 100871, PR China

¹⁰ National Astronomical Observatories, Chinese Academy of Sciences, Beijing 100101, PR China

¹¹ School of Mathematics and Physics, Jinggangshan University, 343009 Ji'an, PR China

¹² School of Astronomy and Space Science, Nanjing University, 210093 Nanjing, PR China

May 30, 2024

ABSTRACT

The kinetic temperature structure of the massive filament DR21 within the Cygnus X molecular cloud complex has been mapped using the IRAM 30 m telescope. This mapping employed the para-H₂CO triplet ($J_{K_a,K_c} = 3_{03}-2_{02}$, $3_{22}-2_{21}$, and $3_{21}-2_{20}$) on a scale of ~ 0.1 pc. By modeling the averaged line ratios of para-H₂CO $3_{22}-2_{21}/3_{03}-2_{02}$ and $3_{21}-2_{20}/3_{03}-2_{02}$ with RADEX under non-LTE assumptions, the kinetic temperature of the dense gas was derived, which ranges from 24 to 114 K, with an average temperature of 48.3 ± 0.5 K at a density of $n(\text{H}_2) = 10^5 \text{ cm}^{-3}$. In comparison to temperature measurements using NH₃ (1,1)/(2,2) and FIR wavelengths, the para-H₂CO (3–2) lines reveal significantly higher temperatures. The dense clumps in various regions appear to correlate with the notable kinetic temperature ($T_{\text{kin}} \geq 50$ K) of the dense gas traced by H₂CO. Conversely, the outskirts of the DR21 filament display lower temperature distributions ($T_{\text{kin}} < 50$ K). Among the four dense cores (N44, N46, N48, and N54), temperature gradients are observed on a scale of ~ 0.1 – 0.3 pc. This suggests that the warm dense gas traced by H₂CO is influenced by internal star formation activity. With the exception of the dense core N54, the temperature profiles of these cores were fitted with power-law indices ranging from -0.3 to -0.5 , with a mean value of approximately -0.4 . This indicates that the warm dense gas probed by H₂CO is heated by radiation emitted from internally embedded protostar(s) and/or clusters. While there is no direct evidence supporting the idea that the dense gas is heated by shocks resulting from a past explosive event in the DR21 region on a scale of ~ 0.1 pc, our measurements of H₂CO towards the DR21W1 region provide compelling evidence that the dense gas in this specific area is indeed heated by shocks originating from the western DR21 flow. Higher temperatures as traced by H₂CO appear to be associated with turbulence on a scale of ~ 0.1 pc. The physical parameters of the dense gas as determined from H₂CO lines in the DR21 filament exhibit a remarkable similarity to the results obtained in OMC-1 and N113 albeit on a scale of approximately 0.1–0.4 pc. This may imply that the physical mechanisms governing the dynamics and thermodynamics of dense gas traced by H₂CO in diverse star formation regions may be dominated by common underlying principles despite variations in specific environmental conditions.

Key words. stars: formation – stars: massive – ISM: clouds – ISM: molecules – radio lines: ISM

1. Introduction

Increasing evidence indicates that the physical properties of the interstellar medium (ISM) have an impact on the star formation rate, the spatial distribution and essential properties of the next generation of stars, such as the elemental composition and initial mass function (e.g., Paumard et al. 2006; Kennicutt 1998a,b; Klessen et al. 2007; Papadopoulos et al. 2011; Zhang et al. 2018; Tang et al. 2019). High-mass stars exert significant influence on their surroundings and subsequent star formation through their

feedback such as outflows, winds, and UV radiation. However, the specifics of the high-mass star formation process and how their feedback affects the initial conditions of high-mass stars during formation are not yet fully understood. To investigate the intricacies or star formation within molecular gas, it is crucial to obtain accurate measurements of its physical properties such as kinetic temperature and volume density.

1.1. DR21 Filament

The Cygnus X molecular cloud complex provides a large sample of star formation regions that exhibit diverse physical conditions and evolutionary stages, making it an ideal laboratory for investigating the process of star formation (e.g., Reipurth & Schneider 2008; Schneider et al. 2010). The DR21 filament at a distance of ~ 1.5 kpc (Rygl et al. 2012) is the densest and most massive region in the entire Cygnus X molecular complex, which is one of the most active star-forming regions within 2 kpc from the Sun (e.g., Schneider et al. 2006; Motte et al. 2007; Davis et al. 2007; Kumar et al. 2007; Beerer et al. 2010; Csengeri et al. 2011). The DR21 filament is an elongated and dense molecular ridge that spans ~ 4 pc in length, extending in a North-South direction. It hosts a mass of $\sim 10^4 M_{\odot}$, which is typically defined by high column densities, i.e., $N(\text{H}_2) > 10^{23} \text{ cm}^{-2}$ (Schneider et al. 2010; Hennemann et al. 2012). The DR21 filament encompasses three prominent regions, namely DR21, DR21(OH), and W75S. Additionally, the DR21W1 region situated to the west of the DR21 region is associated with the western DR21 flow (e.g., Jaffe et al. 1989; Lane et al. 1990; Davis et al. 2007; Zapata et al. 2013). The two well-known star-forming regions DR21 and DR21(OH) are located in the southern and central parts of the DR21 filament, respectively. DR21 is a relatively more evolved massive star-forming region, which harbors a group of luminous H II regions and massive protostars associated with very energetic outflows (e.g., Harris 1973; Garden et al. 1991a; Russell et al. 1992; Kogan & Slysh 1998; Cyganowski et al. 2003; Rygl et al. 2012). The observed outflows in DR21 exhibit a bipolar structure, characterized by its most prominent molecular lobes extending in a northeast-southwest direction (e.g., Davis et al. 2007; Schneider et al. 2010; Skretas et al. 2023). DR21(OH) is an extremely massive star-forming region with intensive maser activity (e.g., Genzel & Downes 1977; Norris et al. 1982; Batrla & Menten 1988; Kogan & Slysh 1998; Harvey-Smith et al. 2008; Schneider et al. 2010). The W75S region, which contains several far-infrared (FIR) sources, is positioned to the north of the DR21 filament (Harvey et al. 1986; Wilson & Mauersberger 1990; Davis et al. 2007; Kumar et al. 2007; Reipurth & Schneider 2008).

Extensive investigations of the DR21 filament have been conducted across various wavelengths, including radio, millimeter, and infrared wavelengths. The region displays a remarkable complexity, with numerous infrared filaments oriented perpendicularly to the ridge, indicating potential sites of star formation as evidenced by observations from the *Spitzer* and *Herschel* telescopes (Marston et al. 2004; Kumar et al. 2007; Beerer et al. 2010; Hennemann et al. 2012). Dust continuum studies reveal a chain of dusty, dense cores along the ridge of the DR21 filament (Chandler et al. 1993; Vallée & Fiege 2006; Motte et al. 2007; Cao et al. 2019). A large number of molecular line observations have been performed, such as in CO, CN, CS, HCN, HCO⁺, CH₃OH, H₂CO, NH₃, and N₂H⁺ (e.g., Wilson & Mauersberger 1990; Vallée & Fiege 2006; Schneider et al. 2006, 2010, 2016; Zapata et al. 2012; Dobashi et al. 2019; Keown et al. 2019; Cao et al. 2022; Bonne et al. 2023; Gong et al. 2023b), which reveal the dynamics and evolution of the dense molecular structure of the DR21 filament on large scales.

The gas temperature structure of the DR21 filament has been mapped in NH₃ (1,1) and (2,2) with the GBT (beam size $\sim 32''$; Keown et al. 2019). The typical kinetic temperature of the dense gas, derived from NH₃ (2,2)/(1,1) line ratios, fall within the range of 20–30 K. In specific regions, the typical gas kinetic temperatures are around 20 K in the W75S region, approximately 22–64 K in the DR21(OH) region, and about 35–

60 K in the DR21W1 region. Mangum et al. (1992) presented high-resolution imaging of the NH₃ (1,1) and (2,2) lines within the DR21(OH) region, utilizing the Very Large Array (VLA) with a beam size of $\sim 4''$. By also analyzing the line ratios of NH₃ (2,2)/(1,1) within dense ammonia cores, they derived the gas kinetic temperatures. These temperatures range from 20 to >80 K, with a typical value of approximately 30 K. The dust temperature structure of the DR21 filament has been derived from spectral energy distribution (SED) fitting to *Herschel* continuum data spanning 70–500 μm (beam size $\sim 40''$; Hennemann et al. 2012; Cao et al. 2019, 2022). The typical dust temperature was found to be between 15 and 31 K, with specific regions exhibiting typical values of 20, 21, 22, 20, 31, 23, 21, 18, and 16 K for W75S FIR 3, W75S FIR 2, W75S FIR 1, DR21(OH)N, DR21(OH), DR21(OH)S, DR21, DR21W1, and DR21S, respectively. These studies provide valuable insights into the gas and dust temperature variations within the DR21 filament. Nevertheless, it is worth noting that the NH₃ (1,1) and (2,2) lines exhibit critical densities on the order of $n_{\text{crit}}(\text{NH}_3) \sim 10^3 \text{ cm}^{-3}$ (Shirley 2015). This characteristic suggests that these particular spectral lines possess a sensitivity suitable for probing the moderate-density gas within molecular clouds. A more comprehensive database of gas temperature which is related to star formation ($n(\text{H}_2) > 10^4 \text{ cm}^{-3}$) in the DR21 filament, with high resolution at a sub-pc scale, is still lacking. Hence, further research and high-resolution observations of the DR21 filament are necessary to achieve a comprehensive characterization of the thermal properties of the dense gas.

1.2. H₂CO as a Temperature Tracer

Formaldehyde (H₂CO), a slightly asymmetric rotor, is ubiquitous in interstellar clouds (e.g., Downes et al. 1980; Hurt et al. 1996; Mühle et al. 2007; Ao et al. 2013; Tang et al. 2013, 2014; Guo et al. 2016; Yan et al. 2019; Brinkmann et al. 2020), exhibits a large number of transitions from centimeter to millimeter wavelengths and is thought to be sensitive to probe physical conditions in various molecular clouds (e.g., Henkel et al. 1980, 1983; Mangum & Wootten 1993; Mangum et al. 2008, 2013a, 2019; Ginsburg et al. 2011, 2016; Ao et al. 2013; Tang et al. 2017a,b, 2018a,b, 2021; Immer et al. 2016). Previous observations of H₂CO indicate that variations in the fractional abundance of H₂CO only rarely exceed one order of magnitude at various stages of star formation (e.g., Mangum et al. 1990, 1993; Caselli et al. 1993; Johnstone et al. 2003; Gerner et al. 2014; Tang et al. 2017a,b, 2018b; Liu et al. 2020). It is possibly the best of the very few molecular thermometers that are available for the analysis of dense molecular gas.

Since the relative populations of the K_a ladders of H₂CO are predominantly governed by collisions, ratios of H₂CO line fluxes involving different K_a ladders can act as good indicators of kinetic temperature, such as para-H₂CO $J_{K_a, K_c} = 3_{22}-2_{21}/3_{03}-2_{02}$, $4_{22}-3_{21}/4_{04}-3_{03}$, and $5_{23}-4_{22}/5_{05}-4_{04}$ (Mangum & Wootten 1993; Tang et al. 2018b; Mazumdar et al. 2022; Kahle et al. 2023). These H₂CO line ratios can accurately trace dense molecular gas as thermometers and have been used to measure the temperature of dense gas in Galactic star formation regions (e.g., Mangum & Wootten 1993; Hurt et al. 1996; Mangum et al. 1999; Watanabe & Mitchell 2008; Nagy et al. 2012; Lindberg et al. 2015; Tang et al. 2017a, 2018a,b; Gieser et al. 2021; Izumi et al. 2023), Galactic center clouds (Qin et al. 2008; Ao et al. 2013; Johnston et al. 2014; Ginsburg et al. 2016; Immer et al. 2016; Lu et al. 2017), and even external galaxies (Mühle et al. 2007; Tang et al. 2017b, 2021; Mangum et al. 2019).

To understand the feedback from the high-mass star-forming process, it is critical to investigate the correlation between the gas temperature and star formation activities in the molecular clouds. The main goal of this paper is to map the kinetic temperature structure of the massive DR21 filament in the north of the Cygnus X molecular cloud complex, making use of the para- H_2CO triplet ($J_{K_a, K_c} = 3_{03-2_{02}}, 3_{22-2_{21}},$ and $3_{21-2_{20}}$, hereafter H_2CO) with a critical density on the order of $n_{\text{crit}}(\text{H}_2\text{CO } 3_{03-2_{02}}) \sim$ a few 10^5 cm^{-3} (Shirley 2015) and to investigate the gas heating mechanism affecting the dense gas in the processes of star formation. In Sects. 2 and 3, we introduce our observations of the H_2CO triplet, data reduction, and results. We discuss the resulting kinetic temperatures derived from H_2CO in Sect. 4. Our main conclusions are summarized in Sect. 5. This paper is part of the "Kinetic temperature of massive star-forming molecular clumps measured with formaldehyde" series of studies exploiting H_2CO as a probe of gas conditions in a variety of Galactic and extragalactic sources.

2. Observations and Data Reduction

Our data presented here were observed with the IRAM 30 m telescope¹ in 2017 May and 2018 October using the HERA receiver (Schuster et al. 2004). The H_2CO ($J_{K_a, K_c} = 3_{03-2_{02}}, 3_{22-2_{21}}$ and $3_{21-2_{20}}$) transitions have rest frequencies of 218.222, 218.475, and 218.760 GHz, respectively, and could be measured simultaneously. At ~ 218 GHz, the beam size is $\sim 12''$ (~ 0.09 pc at 1.5 kpc distance; Rygl et al. 2012). The main beam efficiency and the forward efficiency² are 0.60 and 0.94, respectively. The back-end spectrometer has a bandwidth of ~ 1 GHz and 5377 spectral channels, providing a channel width of $\sim 0.27 \text{ km s}^{-1}$. The central frequency was set to 218.475 GHz. The on-the-fly observing mode was used to measure four $\sim 3 \times 3$ arcmin² maps with steps of $3.5''$ in both right ascension and declination. The surveyed area of the DR21 filament is $\sim 4 \times 10$ arcmin² ($\sim 1.7 \times 4.4 \text{ pc}^2$), centered on $\alpha_{2000} = 20^{\text{h}}39^{\text{m}}01.^{\text{s}}0$ and $\delta_{2000} = 42^{\circ}22'49''.8$.

Data reduction for spectral lines and maps was performed with GILDAS³. To improve the signal-to-noise ratio (S/N) in individual channels, we smoothed contiguous channels to a velocity resolution $\sim 0.8 \text{ km s}^{-1}$ and the spectra were resampled in steps of $\sim 6''$. In total, we acquired 3200 positions corresponding to 3200 spectra for each transition. Nearly 55% of all positions were detected in $\text{H}_2\text{CO } 3_{03-2_{02}}$ and $\sim 23\%$ were also detected in $\text{H}_2\text{CO } 3_{22-2_{21}}$ and $3_{21-2_{20}}$, with S/Ns of $\geq 3\sigma$. We used Gaussian profiles to fit all H_2CO spectra with S/Ns above 3σ . A typical rms noise level (1σ) is $\sim 0.19 \text{ K}$ (T_{mb} scale) at a channel width of 0.8 km s^{-1} .

Generally, $\text{H}_2\text{CO } 3_{22-2_{21}}$ and $3_{21-2_{20}}$ show weaker emissions than $\text{H}_2\text{CO } 3_{03-2_{02}}$. The $\text{H}_2\text{CO } 3_{22-2_{21}}$ and $3_{21-2_{20}}$ transitions have the same K_a ladder and almost the same energy of the upper levels, $E_u \simeq 68 \text{ K}$, above the ground state. They also show similar distributions and line profiles (brightness temperature, linewidth, and velocity in our observations) in star formation regions (e.g., Mangum & Wootten 1993; Tang et al. 2017a,b, 2018a,b, 2021). Furthermore, $\text{H}_2\text{CO } 3_{22-2_{21}}/3_{03-2_{02}}$ and $3_{21-2_{20}}/3_{03-2_{02}}$ line ratios exhibit similar behaviors to trace the kinetic temperature of dense gas (e.g., Mangum & Wootten 1993; Tang et al. 2017a). To further enhance the S/Ns of $\text{H}_2\text{CO } 3_{22-2_{21}}$ and $3_{21-2_{20}}$, we combined the line intensity of two transitions channel by channel.

¹ Based on observations obtained with the IRAM 30 m telescope. IRAM is supported by INSU/CNRS (France), MPG (Germany), and IGN (Spain).

² <https://publicwiki.iram.es/Iram30mEfficiencies>

³ <http://www.iram.fr/IRAMFR/GILDAS>

In the vicinity of DR21(OH), the $\text{H}_2\text{CO } 3_{03-2_{02}}$ spectral lines possess two distinct velocity components. However, identifying these two distinct velocity components becomes difficult for the weaker $\text{H}_2\text{CO } 3_{22-2_{21}}$ and $3_{21-2_{20}}$ lines. To address this, we employed a Gaussian method to fit these ~ 70 positions that clearly exhibit two velocity components. The two velocity components measured using $\text{H}_2\text{CO } 3_{03-2_{02}}$ are approximately at local standard of rest velocities (V_{LSR}) of -4 and -2 km s^{-1} , consistent with previous findings from observations of HCO^+ , H^{13}CO^+ , and N_2H^+ (Schneider et al. 2010; Cao et al. 2022; Bonne et al. 2023). High-resolution observations revealed that these two velocity components were attributed to two closely aligned fibers in the DR21(OH)/W75S region (Cao et al. 2022). Subsequently, we combined the data from these two velocity components based on the integrated intensity ratio between each pair of velocity component lines. Hence, the gas temperatures of these positions in the two velocity components were not determined individually.

3. Results

3.1. Overview

The velocity-integrated intensity distributions of the H_2CO triplet and the combined $\text{H}_2\text{CO } 3_{22-2_{21}}$ and $3_{21-2_{20}}$ lines in the DR21 filament ($V_{\text{LSR}} = -10$ to 4 km s^{-1}) are shown in Fig. 1. The intensity-weighted velocity field (moment 1), linewidth (moment 2), and channel maps of $\text{H}_2\text{CO } 3_{03-2_{02}}$ are shown in Figs. 2 and A.1. The observed H_2CO spectra of sixteen dense cores identified with 1.2 mm continuum emission by Motte et al. (2007) are shown in Fig. 3. The locations of these dense cores in the DR21 filament are indicated in Fig. 4 (left panel) and are listed in Table 1. The parameters of the Gaussian fits, which include velocity-integrated intensity, $\int T_{\text{mb}} dv$, local standard of rest velocity, V_{LSR} , full width at half maximum (FWHM) line width, and peak temperature (T_{mb}) of the H_2CO spectra in these dense cores are listed in Table 1. Three dense cores, namely N35, N45, and N52, situated at the periphery of the DR21 filament, exhibit weak emissions of $\text{H}_2\text{CO } 3_{22-2_{21}}$ and $3_{21-2_{20}}$ with S/Ns below 3σ , as depicted in Figs. 1 and 4. Consequently, these cores were omitted from Fig. 3.

3.2. Distribution of H_2CO

The $\text{H}_2\text{CO } 3_{03-2_{02}}$ line exhibits an extensive distribution and provides a clear picture of the dense ridge structure of the DR21 filament (see the left panel of Fig. 1). It illuminates notable dense molecular structures including the DR21, DR21(OH), and W75S regions on a linear scale of ~ 0.1 pc. Obviously, the strongest emission of H_2CO is associated with the two most active star-forming regions, DR21 and DR21(OH). These results are consistent with prior observational findings using other dense gas tracers, such as CN, C^{18}O , CS, HCN, and HCO^+ (Schneider et al. 2010; Dobashi et al. 2019). The spatial distribution of $\text{H}_2\text{CO } 3_{03-2_{02}}$ illustrates a close correspondence with the spatial distribution of the dust emission at wavelengths of $850 \mu\text{m}$ and 1.2 mm , including the presence of dense ridge structures and dust emission peaks within the DR21 filament (Davis et al. 2007; Motte et al. 2007; Ching et al. 2022), which confirms previous observational results regarding massive star formation regions (e.g., Tang et al. 2017a, 2018a,b, 2021). In contrast, $\text{H}_2\text{CO } 3_{22-2_{21}}$ and $3_{21-2_{20}}$ indicate less extended distributions and are only detectable in the densest areas of the DR21 filament, as shown in the rightmost three panels of Fig. 1.

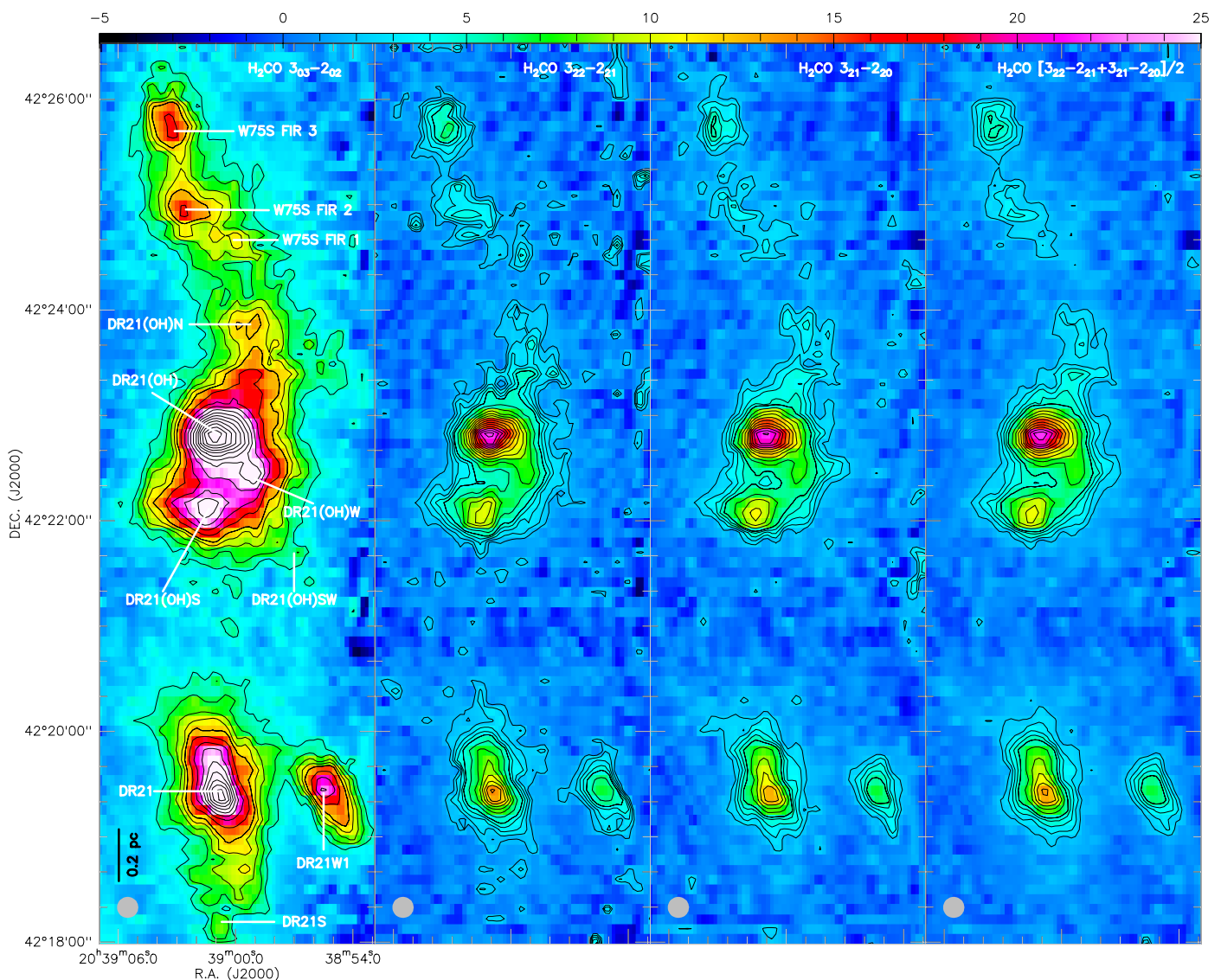


Fig. 1. Velocity-integrated intensity maps (T_{mb} scale; color bar in units of K km s^{-1}) of $\text{H}_2\text{CO } 3_{03-2_{02}}$ (left), $3_{22-2_{21}}$ (center-left), $3_{21-2_{20}}$ (center-right), and averaged $3_{22-2_{21}}$ and $3_{21-2_{20}}$ (right), integrated from $V_{\text{LSR}} = -10$ to 4 km s^{-1} of the DR21 filament. Contour levels are from 4.8 to 12 K km s^{-1} with steps of 1.8 K km s^{-1} and from 12 to 59 K km s^{-1} with steps of 3.6 K km s^{-1} for $\text{H}_2\text{CO } 3_{03-2_{02}}$, and from 1.7 to 4.4 K km s^{-1} with steps of 0.66 K km s^{-1} and from 4.3 to 21.2 K km s^{-1} with steps of 1.3 K km s^{-1} for $\text{H}_2\text{CO } 3_{22-2_{21}}$, $3_{21-2_{20}}$, and combined $3_{22-2_{21}}$ and $3_{21-2_{20}}$. The locations of source names are taken from Davis et al. (2007), Reipurth & Schneider (2008), and Ching et al. (2022).

The intensity-weighted velocity (moment 1) and channel maps of $\text{H}_2\text{CO } (3_{03-2_{02}})$ reveal the complex velocity field of the DR21 filament (see the left panels of Figs. 2 and A.1). Notably, multiple velocity gradients traverse the primary DR21 filament as well as the DR21W1 region. The W75S region shows an increasing gradient of velocity (-4.5 to -2.5 km s^{-1}) that extends from the northeast to the southwest, while the DR21(OH) region displays a decreasing northwest-southeast velocity gradient (-2.5 to -4.0 km s^{-1}). Utilizing high-resolution observations of H^{13}CO^+ , N_2H^+ , and NH_2D toward the W75S/DR21(OH) region (beam size $\sim 5''$), it has been observed that three nearly parallel fibers exist at distinct velocities, primarily aligned in a north-south orientation (Cao et al. 2022). Such an alignment may give rise to the complex velocity field found within this region. Furthermore, the DR21 and DR21W1 regions exhibit a comparable increasing northeast-to-southwest velocity gradient with the mean velocity ranging from -3.5 to -1.5 km s^{-1} and from -5.0 to -2.0 km s^{-1} , respectively. Our observed H_2CO results corrob-

orate previous observational outcomes obtained from H^{13}CO^+ , C^{34}S , and N_2H^+ (Schneider et al. 2010).

As shown in the right panel of Fig. 2, higher linewidths ($\geq 3 \text{ km s}^{-1}$) are typically associated with dense clumps, such as DR21, DR21W1, DR21(OH), DR21(OH)S, and DR21(OH)W, in the two most active star-forming regions DR21 and DR21(OH). Moderate linewidths ($2-3 \text{ km s}^{-1}$) are distributed in the dense clumps of the W75S region, as well as around the dense clumps of the DR21 and DR21(OH) regions, while lower linewidths ($< 2 \text{ km s}^{-1}$) are located on the outskirts of the DR21 filament. The fitted linewidth of $\text{H}_2\text{CO } (3_{03-2_{02}})$ ranges from 1.7 to 10.4 km s^{-1} with an average of $\sim 3.8 \pm 0.1 \text{ km s}^{-1}$ (errors given here and elsewhere are standard deviations of the mean).

3.3. Line Ratios of H_2CO

As mentioned in Sects. 1 and 2, $\text{H}_2\text{CO } 3_{22-2_{21}}/3_{03-2_{02}}$ and $3_{21-2_{20}}/3_{03-2_{02}}$ line ratios exhibit similar behaviors in delineating

the kinetic temperature of the dense gas (e.g., Mangum & Wootten 1993; Tang et al. 2017a). The present study employs the averaged ratio of $\text{H}_2\text{CO } 0.5 \times [(3_{22}-2_{21} + 3_{21}-2_{20})/3_{03}-2_{02}]$ (obtained from the combined $\text{H}_2\text{CO } 3_{22}-2_{21}$ and $3_{21}-2_{20}$ to $\text{H}_2\text{CO } 3_{03}-2_{02}$ ratio) as an indicator of the kinetic temperature. Substantially, higher H_2CO line ratios typically correspond to higher kinetic temperatures (Ao et al. 2013; Ginsburg et al. 2016; Tang et al. 2018a, 2021). Thus, the ratio maps may function as a proxy for the relative kinetic temperature. The line ratio map of the DR21 filament is shown in the left panel of Fig. 4. The line ratios are calculated by velocity-integrated intensities where the combined $\text{H}_2\text{CO } 3_{22}-2_{21}$ and $3_{21}-2_{20}$ lines are detected with S/Ns of $\geq 3\sigma$. The H_2CO line ratios range from 0.08 to 0.42 with an average value of 0.22 ± 0.01 in the DR21 filament. Higher H_2CO line ratios (>0.35) have been observed in association with dense clumps, such as W75S FIR 3, DR21(OH), DR21(OH)S, DR21, and DR21W1. Moderate line ratios ranging from 0.2 to 0.35 are prevalent throughout the vicinity of these dense clumps. Notably, the outskirts of the DR21 and the area located between DR21(OH) and W75S exhibit relatively lower line ratios (<0.2).

3.4. Kinetic Temperatures Derived from H_2CO Line Ratios

As described in Sects. 2 and 3.3, the determination of the kinetic temperature involves calculating the averaged ratio of $\text{H}_2\text{CO } 0.5 \times [(3_{22}-2_{21} + 3_{21}-2_{20})/3_{03}-2_{02}]$. To model the relationship between the gas kinetic temperature and the measured average of $\text{H}_2\text{CO } 0.5 \times [(3_{22}-2_{21} + 3_{21}-2_{20})/3_{03}-2_{02}]$ ratios, we employed the RADEX⁴ non-LTE model (van der Tak et al. 2007) with collision rates provided by Wiesenfeld & Faure (2013). In Fig. B.1, we adopted a background temperature of 2.73 K, an average measured linewidth of 3.8 km s^{-1} , and a column density of $N(\text{para-H}_2\text{CO}) = 6.6 \times 10^{13} \text{ cm}^{-2}$. The impact of different column densities of H_2CO on the kinetic temperature is found to be minimal when all lines are optically thin, as shown in Fig. 3 in Tang et al. (2017b) or Fig. 4 in Tang et al. (2018a). Additionally, opacities within dense massive star-forming clumps have little effect on the kinetic temperature (Ginsburg et al. 2016; Immer et al. 2016; Tang et al. 2017b, 2018b). We assume that para- H_2CO (3–2) is optically thin in DR21 (see below for detailed arguments). The measured H_2 number densities, $n(\text{H}_2)$, of massive dense cores in DR21 range from $\sim 10^4$ to 10^6 cm^{-3} (Schneider et al. 2006; Jakob et al. 2007; Cao et al. 2019, 2022). Previous observations have demonstrated that para- H_2CO (3–2) is particularly sensitive to the gas density at $\sim 10^5 \text{ cm}^{-3}$ (Ginsburg et al. 2016; Immer et al. 2016; Tang et al. 2017b, 2021). Therefore, we adopt an average spatial gas density of 10^5 cm^{-3} for the DR21 filament. By utilizing the methodology outlined in Sect. 3.1 of Tang et al. (2017b), we can calculate the average column density $N(\text{para-H}_2\text{CO})$ of the entire DR21 region based on the H_2CO ($3_{03}-2_{02}$) average brightness temperature. The resulting value is $6.6 \times 10^{13} \text{ cm}^{-2}$ at a volume density of approximately 10^5 cm^{-3} . Previous observations of para- H_2CO (3–2 and 4–3) toward dense clumps representing various evolutionary stages of high-mass star formation in the Galactic plane suggest an averaged fractional abundance of para- H_2CO of $\sim 3.9 \times 10^{-10}$ (Tang et al. 2018b). The average column density of H_2 , $N(\text{H}_2)$, in the DR21 ridge, where the distribution of $N(\text{H}_2)$ agrees well with that of our H_2CO ($3_{03}-2_{02}$) lines, is $\sim 4.2 \times 10^{23} \text{ cm}^{-2}$ as determined from the *Herschel* 70–500 μm continuum data (Hennemann et al. 2012). Subsequently, we can compute a typical fractional abundance of para- H_2CO of roughly 1.6×10^{-10} in the

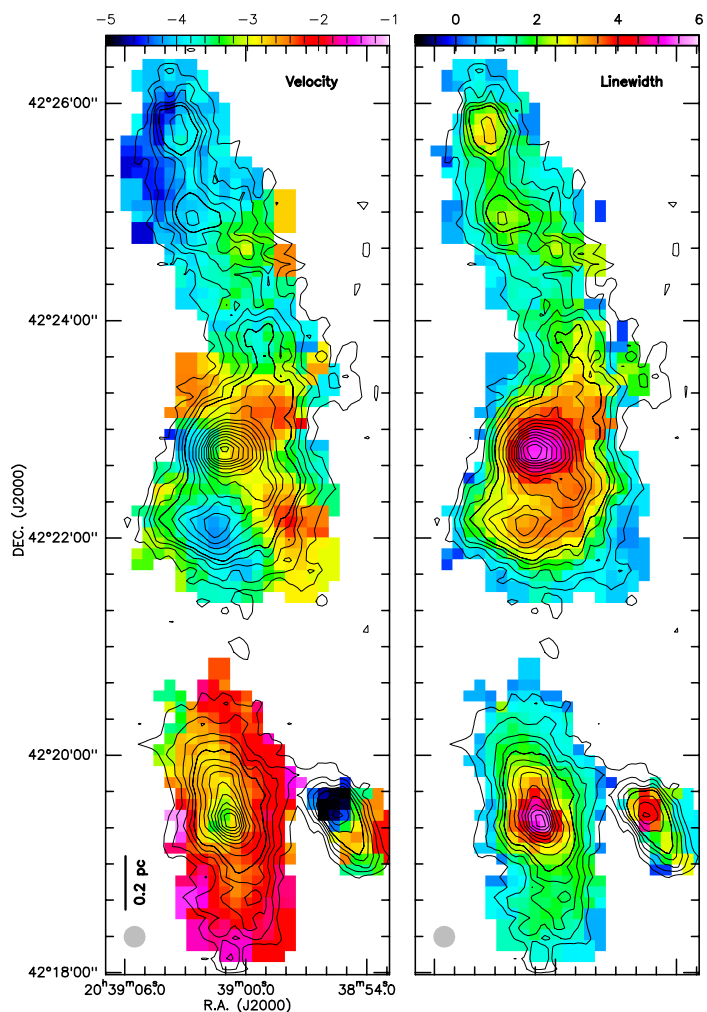


Fig. 2. The intensity-weighted velocity field (moment 1, left) and linewidth (moment 2, right) of $\text{H}_2\text{CO } 3_{03}-2_{02}$. The unit of each colour bar is km s^{-1} . Contours are $\text{H}_2\text{CO } 3_{03}-2_{02}$ integrated intensities (same as in Fig. 1).

DR21 filament using the above-mentioned average H_2CO column density of the entire DR21 region, which is in agreement with previous observational results in high-mass star formation regions (Tang et al. 2018b). This supports the reasonability of our RADEX calculations using the average column density $N(\text{para-H}_2\text{CO})$ in the DR21 region.

Pertaining to kinetic temperatures, it has been observed that subtle variations occur across different column densities at a given H_2 number density of 10^5 cm^{-3} (Tang et al. 2018a). Specifically, we explored this relationship at column densities of $N(\text{para-H}_2\text{CO}) = 1.0 \times 10^{13}$, 6.6×10^{13} , and $1.0 \times 10^{14} \text{ cm}^{-2}$, as depicted in Fig. B.1. It indicates that there exists a slight temperature variation corresponding to different column densities. The temperature differences derived from column densities of $N(\text{para-H}_2\text{CO}) = 1.0 \times 10^{13}$ and $1.0 \times 10^{14} \text{ cm}^{-2}$, compared to $6.6 \times 10^{13} \text{ cm}^{-2}$, are found to be smaller than the uncertainties in temperature determined from the errors associated with observed H_2CO line ratios. Therefore we employed the established correlation between H_2CO line ratios and kinetic temperature at a spatial density of 10^5 cm^{-3} and a column density of $6.6 \times 10^{13} \text{ cm}^{-2}$ in order to convert the ratio maps into temperature maps in this work. These transformed temperature maps are

⁴ <http://var.sron.nl/radex/radex.php>

illustrated in Fig. 4. As previously stated, the measured H_2 number densities of massive dense cores within DR21 span from approximately $\sim 10^4$ to 10^6 cm^{-3} . Regarding kinetic temperatures, subtle variations have been noted across different number densities within the range of $\sim 10^4$ to 10^6 cm^{-3} (see Fig. 5 in Tang et al. 2021). It appears that at $n(\text{H}_2) = 10^5 \text{ cm}^{-3}$, T_{kin} consistently exhibits lower values compared to those at 10^4 to 10^6 cm^{-3} by approximately $\lesssim 35\%$ for $T_{\text{kin}} \lesssim 100 \text{ K}$ in Fig. 4.

The applicability of local thermodynamic equilibrium (LTE) as a reliable approximation for H_2CO level populations has been established under certain conditions, namely when the corresponding transitions are optically thin and the targets are characterized by high densities (Mangum & Wootten 1993). By employing the methodology outlined in Tang et al. (2017b) (refer to their Eq. 2) and utilizing the RADEX model, we conducted a comprehensive analysis to investigate the relationship between kinetic temperature and the combined H_2CO ratio within the LTE regime in Fig. B.1. It indicates a satisfactory agreement between the temperatures obtained from the LTE model and those derived from the RADEX model, under the condition of a spatial gas density of $n(\text{H}_2) = 10^5 \text{ cm}^{-3}$, as long as the kinetic temperature remains below 100 K.

The kinetic temperature of the warm dense gas in the DR21 region, as indicated by the H_2CO line ratios, ranges from 24 to 114 K, with an average temperature of $48.3 \pm 0.5 \text{ K}$ at a density of $n(\text{H}_2) = 10^5 \text{ cm}^{-3}$ (see also Table 2). As shown in Fig. 4 and Table 3, it reveals the inhomogeneous temperature distribution of the DR21 region across different sub-regions of the molecular complex. The H_2CO line ratio analysis demonstrates that two dense clumps, DR21(OH) and DR21(OH)S, located within the central parts of the DR21 filament, exhibit noticeably high temperatures exceeding 100 K. The kinetic temperatures of the dense clumps W75S FIR 3, DR21, and DR21W1, albeit lower than in DR21(OH), remain relatively high ranging between 77 to 84 K. Conversely, the gas temperatures of the dense clumps W75S FIR 1, W75S FIR 2, DR21(OH)N, DR21(OH)W, and DR21S span the range from 38 to 57 K. Table 1 provides a summary of the detailed temperature results for all sixteen dense cores apparent in the DR21 filament. In the immediate vicinity of the dense regions such as W75S FIR 3, W75S FIR 2, DR21(OH), DR21(OH)S, and DR21, the kinetic temperatures range between 30 to 45 K. The region located between DR21(OH) and W75S and the outskirts of the DR21 filament exhibit significantly lower temperatures below 40 K.

To address the impact of $\text{H}_2\text{CO}(3-2)$ line saturation on our temperature measurements, we employed the RADEX non-LTE model. This model allowed us to calculate the opacities of $\text{H}_2\text{CO}(3-2)$ lines, adopting an average temperature of $T_{\text{kin}} = 48 \text{ K}$, an average measured linewidth of 3.8 km s^{-1} , an H_2CO column density of $N(\text{para-}\text{H}_2\text{CO}) = 6.6 \times 10^{13} \text{ cm}^{-2}$, and a gas volume density of $n(\text{H}_2) = 10^5 \text{ cm}^{-3}$. The resulting optical depths for the $\text{H}_2\text{CO} 3_{03-2_{02}}$, $3_{22-2_{21}}$, and $3_{21-2_{20}}$ transitions were approximately 1.2, 0.28, and 0.28, respectively. These values suggest that in the location of the dense cores, opacities in the $\text{H}_2\text{CO} 3_{03-2_{02}}$ lines may exhibit slight saturation, potentially leading to a slight overestimation of kinetic temperatures by $\sim 20\%$.

3.5. Thermal and Non-thermal Motions Obtained from H_2CO

The thermal and non-thermal linewidths (Pan & Padoan 2009; Dewangan et al. 2016), represented by $\sigma_{\text{T}} = \sqrt{\frac{kT_{\text{kin}}}{m_{\text{H}_2\text{CO}}}}$

and $\sigma_{\text{NT}} = \sqrt{\frac{\Delta v^2}{8 \ln 2} - \sigma_{\text{T}}^2} \approx \Delta v / 2.355$, respectively, are determined based on the kinetic temperature derived from the H_2CO line ratios. In this context, k denotes the Boltzmann constant, T_{kin} corresponds to the kinetic temperature of the gas, $m_{\text{H}_2\text{CO}}$ represents the mass of a formaldehyde molecule, and Δv signifies the measured FWHM linewidth of $\text{H}_2\text{CO} 3_{03-2_{02}}$. As mentioned in Sect. 2, approximately 70 positions in the DR21(OH) region exhibit two distinct velocity components at about -2 and -4 km s^{-1} (see also Fig. 3). Additionally, determining the individual gas temperatures for these positions in the two velocity components proved to be challenging. Hence, in this study, we employ the approach of utilizing the averaged linewidth, which is weighted by the integrated intensity of $\text{H}_2\text{CO} 3_{03-2_{02}}$. By analyzing the data, the thermal linewidth ranges from 0.08 to 0.18 km s^{-1} with an average value of $0.11 \pm 0.01 \text{ km s}^{-1}$, whereas the non-thermal linewidth spans from 0.74 to 4.40 km s^{-1} with an average value of $1.60 \pm 0.02 \text{ km s}^{-1}$ (see also Table 2). It is apparent that the non-thermal linewidth significantly exceeds the thermal linewidth, indicating that the dense gas traced by H_2CO is primarily governed by non-thermal motions. These findings align with previous studies conducted on star-forming regions in our Galaxy and the Large Magellanic Cloud using H_2CO ($J=3-2$ and $4-3$) observations (Tang et al. 2017a, 2018a,b, 2021).

The non-thermal linewidth distribution of $\text{H}_2\text{CO} 3_{03-2_{02}}$ is depicted in Fig. 4, showing similarities with the H_2CO linewidth observed in the W75S and DR21 regions. However, a significant disparity in the distribution of non-thermal linewidth and H_2CO linewidth is observed in the DR21(OH) region, as illustrated in Fig. 2. As mentioned above, the lower values for the non-thermal linewidth in the DR21(OH) region can be attributed to the averaging of linewidths derived from the two distinct velocity components. In the western region of DR21(OH)N, weak H_2CO emission is detected, as depicted in Fig. 2. At many positions in this region, two velocity components are present, but one of them exhibits lower S/Ns, making it challenging to identify it as a significant signal. Consequently, we employed a single Gaussian velocity component to fit the H_2CO lines in this specific area, resulting in higher non-thermal linewidths in the western region of DR21(OH)N.

Distributions of the Mach number (given as $\mathcal{M} = \sigma_{\text{NT}}/a_s$, $a_s = \sqrt{\frac{kT_{\text{kin}}}{\mu m_{\text{H}}}}$, where $\mu = 2.37$ is the mean molecular weight for molecular clouds and m_{H} is the mass of a hydrogen atom) of the DR21 filament is shown in Fig. 4. The Mach number ranges from 1.9 to 10.3 with an average of 4.0 ± 0.1 (see also Table 2). This suggests that supersonic non-thermal motions (e.g., turbulence, outflows, shocks, and/or magnetic fields) are dominant in the dense gas traced by H_2CO . The DR21W1 region, linked to the western DR21 flow, exhibits particularly high Mach numbers ($\mathcal{M} \sim 10$) as evidenced by previous studies (e.g., Jaffe et al. 1989; Lane et al. 1990; Davis et al. 2007; Zapata et al. 2013). This association indicates a strong influence of shocks on the dense gas traced by H_2CO . Within the dense core of the DR21 region, the Mach numbers are approximately $\mathcal{M} \sim 7$, while in the W75S FIR 3 region, they are around $\mathcal{M} \sim 6$, slightly lower than those observed in the DR21W1 region. This observation of high Mach numbers suggests that local star formation activities (e.g., outflows, shocks; Davis et al. 2007; Motte et al. 2007; Schneider et al. 2010) in the DR21 and W75S FIR 3 regions may impact the dense gas. In the DR21(OH) region, the Mach numbers are lower (2–3), whereas in the western region of DR21(OH)N, they are higher (6–7). These variations are attributed to the two velocity components mentioned in the above paragraph. Moving

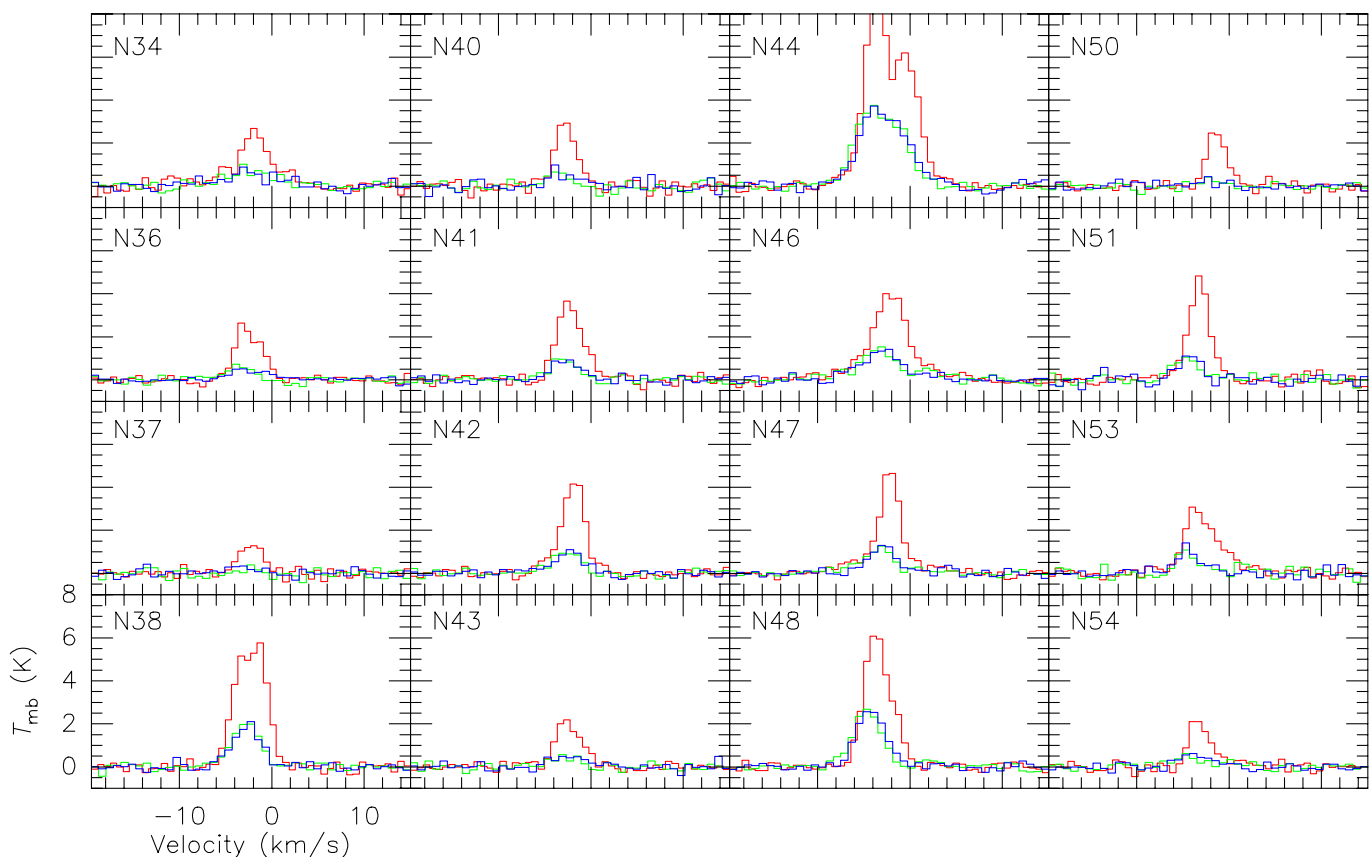


Fig. 3. Observed H_2CO spectra of the dense cores in the DR21 filament obtained with the IRAM 30 m. Red, green, and blue lines show H_2CO $3_{03}-2_{02}$, $3_{21}-2_{20}$, and $3_{22}-2_{21}$, respectively. The dense cores, identified through 1.2 mm continuum emission as described by Motte et al. (2007), are referenced for nomenclature, positions, and physical parameters in Table 1.

towards the outskirts and extended regions of the DR21 filament, the typical Mach number ranges from 2 to 4.

4. Discussion

4.1. Comparison of Temperatures Derived from H_2CO , NH_3 , and CO

Ammonia (NH_3) is widely recognized as a standard temperature tracer for dense molecular gas (e.g., Ho & Townes 1983). Its unique properties make it an invaluable tool for studying the thermal characteristics of various molecular environments (e.g., Henkel et al. 1987, 2008; Molinari et al. 1996; Jijina et al. 1999; Dunham et al. 2011; Wang et al. 2012; Wielen et al. 2012; Mangum et al. 2013b; Lu et al. 2014, 2017; Ott et al. 2014; Gong et al. 2015a,b; Krieger et al. 2017; Sokolov et al. 2018; Wang et al. 2023; Zhang et al. 2024). In order to investigate the temperature variations across various layers of the molecular cloud, we conducted a comparative analysis between our results of gas temperature derived from H_2CO (3–2) (with $n_{\text{crit}}(\text{H}_2\text{CO } 3_{03}-2_{02}) \sim \text{few } 10^5 \text{ cm}^{-3}$, Shirley 2015) and the previous measurements using NH_3 (J, K) = (1,1) and (2,2) (with $n_{\text{crit}}(\text{NH}_3) \sim 10^3 \text{ cm}^{-3}$, Shirley 2015), specifically within the DR21 filament. As mentioned in Sect. 1.1, the temperature distribution of gas within the DR21 filament has been charted using NH_3 (1,1) and (2,2) with the GBT (beam size $\sim 32''$; Keown et al. 2019). Analysis of the NH_3 (2,2)/(1,1) line ratios has shown that the kinetic temperature of the dense gas typically ranges between 20 and 30 K. However, there are variations in temperature across different regions (see Table 3). Specifically, the

W75S region has a typical temperature of about 20 K, while the DR21(OH) region has temperatures ranging from 22 to 64 K, and the DR21W1 region has temperatures around 35–60 K. High-resolution imaging of the NH_3 (1,1) and (2,2) lines within the DR21(OH) region was presented by Mangum et al. (1992), using the VLA with a beam size of $\sim 4''$ ($\sim 0.03 \text{ pc}$ at 1.5 kpc distance). The gas kinetic temperatures of dense ammonia cores derived from line ratios of NH_3 (2,2)/(1,1) range from 20 to $>80 \text{ K}$, with a typical value of $\sim 30 \text{ K}$. On a larger scale of $\sim 0.23 \text{ pc}$, the temperature distribution derived from our H_2CO (3–2) data exhibits similarities to that obtained from NH_3 (1,1) and (2,2). Notably, our analysis of H_2CO (3–2) consistently reveals higher gas temperatures compared to NH_3 (1,1) and (2,2), both within dense clumps and across extended regions of the DR21 filament (see Sect. 3.4 and Table 1). These findings align with previous observations in star-forming regions of the Milky Way, the Large Magellanic Cloud, and our Galactic center clouds (Tang et al. 2017a,b, 2018a,b, 2021; Ginsburg et al. 2016).

Observations conducted using the KOSMA 3 m telescope have provided insights into the gas properties within the DR21 filament region through the analysis of low- to high- J CO lines on a spatial scale of $\sim 0.4 \text{ pc}$ (Jakob et al. 2007). These observations reveal the presence of two distinct gas components (see Table 3). The cold component exhibits a kinetic temperature ranging from 30 to 40 K, while the warm component displays temperatures ranging from 80 to 150 K in regions such as W75S FIR 1, DR21(OH), DR21, and DR21W1, at densities of $n(\text{H}_2) \sim 10^4-10^6 \text{ cm}^{-3}$. Furthermore, in these regions, the gas temperatures derived from H_2CO line ratios range from 50 to 114 K on a spatial scale of $\sim 0.1 \text{ pc}$. Notably, these values align closely with the

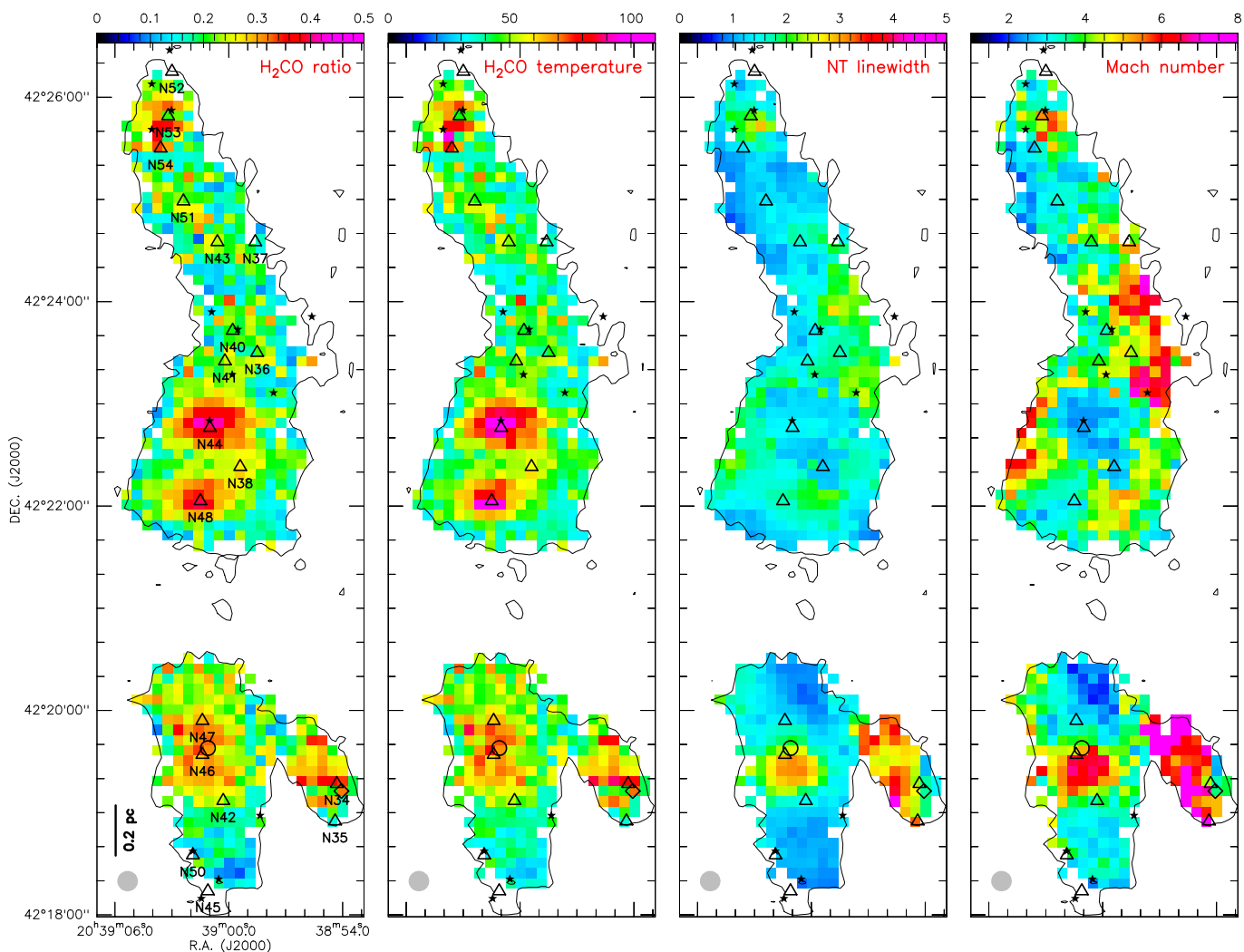


Fig. 4. Left two panels: The averaged velocity-integrated intensity ratio map of $\text{H}_2\text{CO } 0.5 \times [(3_{22-2_{21}} + 3_{21-2_{20}}) / 3_{03-2_{02}}]$ in the DR21 filament (see Sect. 3). The kinetic temperatures derived from the H_2CO line ratios (color bar in units of K). Right two panels: Maps of non-thermal linewidth (color bar in units of km s^{-1}) and Mach number. The black stars and triangles show the locations of protostars (Davis et al. 2007) and the dense cores (Motte et al. 2007), respectively. The black circle and diamond illustrate the locations of the explosion center as described by Zapata et al. (2013) and the infrared-quiet massive dense core as delineated by Cao et al. (2019), respectively. Black contours show the integrated intensity of $\text{H}_2\text{CO } 3_{03-2_{02}}$ at 4.8 K km s^{-1} (see Fig. 1).

temperatures obtained from the warm gas component identified through the analysis of CO lines.

The observed disparities likely arise from temperature gradients, as H_2CO and NH_3 may probe distinct regions within star-forming regions. The H_2CO (3–2) lines emerge as an interesting tool for detecting the presence of warm and dense molecular gas within star-forming regions. These transitions are highly sensitive to environments where the gas temperature is elevated, making it an ideal tracer of energetic conditions associated with active star formation. In contrast, the NH_3 (1,1) and (2,2) transitions are well-suited for probing the cooler and less dense molecular gas prevalent in these regions. It would be intriguing to conduct mapping of the region using higher excited NH_3 transitions (e.g., Henkel et al. 1987, 2008; Mangum et al. 2013b; Lu et al. 2017; Gong et al. 2015a,b; Krieger et al. 2017). This approach would also serve as a valuable tool to verify the authenticity of the high temperatures, ensuring that they are not a result of slightly saturated $\text{H}_2\text{CO } 3_{03-2_{02}}$ lines.

4.2. Comparison of Temperatures Obtained from Gas and Dust

Gas temperature refers to the kinetic temperature of the gas particles, while dust temperature reflects the thermal equilibrium of the dust grains. The investigation of gas and dust temperatures in molecular clouds is of paramount importance in understanding the physical conditions within these regions. It is commonly expected that gas and dust are thermally coupled in dense regions ($n(\text{H}_2) \gtrsim 10^4 \text{ cm}^{-3}$) due to the increased frequency of interactions between these two components (Goldsmith 2001). Previous observations with NH_3 (1,1) and (2,2) lines have consistently demonstrated that the temperatures derived from gas and dust (derived at far-infrared wavelengths) measurements are typically in concordance within the active dense clumps found in Galactic disk clouds (e.g., Dunham et al. 2010; Giannetti et al. 2013; Battersby et al. 2014; Merello et al. 2019; Tursun et al. 2020; Zhang et al. 2024). However, it should be noted that gas temperatures obtained from H_2CO (3–2 and 4–3) lines do not exhibit agreement with FIR-derived dust measurements in both our Galactic star-forming regions (Tang et al. 2017a, 2018a,b) and Galactic

Table 1. Parameters of dense cores in DR21 filament.

Dense core	Offset ", "	Transition	$\int T_{\text{mb}} dv$ K km s ⁻¹	V_{LSR} km s ⁻¹	FWHM km s ⁻¹	T_{mb} K	σ_{T} km s ⁻¹	σ_{NT} km s ⁻¹	c_s km s ⁻¹	M	T_{kin} K	T_{turb} K
N34	-71.5, -211.5	$3_{03}-2_{02}$	13.0 (0.8)	-2.4 (0.1)	5.4 (0.5)	2.3	0.15 (0.01)	2.30 (0.20)	0.54 (0.05)	4.3	84 (15)	70
		$(3_{21}-2_{20}+3_{22}-2_{21})/2$	4.6 (0.4)	-2.4 (0.3)	6.9 (0.7)	0.6						
N36	-29.5, 40.5	$3_{03}-2_{02}$	10.2 (0.4)	-3.2 (0.1)	4.0 (0.2)	2.4	0.11 (0.01)	1.68 (0.07)	0.40 (0.02)	4.2	46 (5)	43
		$(3_{21}-2_{20}+3_{22}-2_{21})/2$	2.2 (0.2)	-3.2 (0.2)	3.8 (0.5)	0.5						
N37	-29.5, 106.5	$3_{03}-2_{02}$	5.0 (0.4)	-2.8 (0.1)	3.5 (0.3)	1.4	0.10 (0.01)	1.47 (0.13)	0.36 (0.04)	4.0	38 (7)	36
		$(3_{21}-2_{20}+3_{22}-2_{21})/2$	0.8 (0.2)	-2.9 (0.4)	3.1 (0.8)	0.3						
N38	-17.5, -25.5	$3_{03}-2_{02}$	27.9 (2.5)	-2.9 (0.1)	2.7 (0.2)	4.8	0.13 (0.01)	1.15 (0.07)	0.44 (0.02)	2.6	57 (6)	50
		$(3_{21}-2_{20}+3_{22}-2_{21})/2$	7.5 (0.2)	-2.9 (0.1)	3.0 (0.2)	1.2						
N40	-11.5, 52.5	$3_{03}-2_{02}$	9.9 (0.5)	-3.5 (0.1)	3.1 (0.2)	3.0	0.11 (0.01)	1.32 (0.08)	0.39 (0.03)	3.4	44 (7)	41
		$(3_{21}-2_{20}+3_{22}-2_{21})/2$	2.0 (0.4)	-3.5 (0.2)	2.8 (0.6)	0.7						
N41	-11.5, 34.5	$3_{03}-2_{02}$	14.5 (0.5)	-2.8 (0.1)	3.5 (0.2)	3.5	0.12 (0.01)	1.64 (0.06)	0.42 (0.01)	3.9	51 (3)	47
		$(3_{21}-2_{20}+3_{22}-2_{21})/2$	3.5 (0.2)	-2.9 (0.1)	3.4 (0.2)	1.0						
N42	-5.5, -223.5	$3_{03}-2_{02}$	15.8 (0.4)	-2.4 (0.1)	3.5 (0.1)	4.3	0.12 (0.01)	1.47 (0.04)	0.43 (0.02)	3.5	52 (4)	47
		$(3_{21}-2_{20}+3_{22}-2_{21})/2$	3.9 (0.3)	-2.5 (0.1)	3.6 (0.3)	1.0						
N43	-5.5, 106.5	$3_{03}-2_{02}$	8.6 (0.4)	-3.1 (0.1)	3.8 (0.2)	2.1	0.12 (0.01)	1.62 (0.08)	0.42 (0.03)	3.9	50 (8)	46
		$(3_{21}-2_{20}+3_{22}-2_{21})/2$	2.0 (0.3)	-2.7 (0.3)	3.9 (0.7)	0.5						
N44	0.5, -1.5	$3_{03}-2_{02}$	54.7 (1.4)	-2.9 (0.1)	3.4 (0.1)	8.0	0.17 (0.01)	1.43 (0.04)	0.60 (0.04)	2.4	103 (15)	78
		$(3_{21}-2_{20}+3_{22}-2_{21})/2$	21.8 (1.6)	-3.0 (0.6)	3.6 (0.6)	3.0						
N46	6.5, -193.5	$3_{03}-2_{02}$	22.4 (0.6)	-2.8 (0.1)	5.5 (0.2)	3.9	0.15 (0.01)	2.32 (0.08)	0.52 (0.02)	4.5	77 (7)	66
		$(3_{21}-2_{20}+3_{22}-2_{21})/2$	7.6 (0.4)	-3.2 (0.1)	5.6 (0.4)	1.3						
N47	6.5, -175.5	$3_{03}-2_{02}$	16.2 (0.5)	-2.8 (0.1)	3.3 (0.1)	4.7	0.13 (0.01)	1.38 (0.06)	0.47 (0.02)	3.0	63 (5)	54
		$(3_{21}-2_{20}+3_{22}-2_{21})/2$	4.7 (0.3)	-3.2 (0.1)	3.7 (0.3)	1.2						
N48	6.5, -49.5	$3_{03}-2_{02}$	26.1 (0.4)	-4.4 (0.1)	4.1 (0.1)	6.0	0.17 (0.01)	1.73 (0.03)	0.59 (0.02)	2.9	100 (5)	77
		$(3_{21}-2_{20}+3_{22}-2_{21})/2$	10.3 (0.2)	-4.4 (0.1)	3.6 (0.1)	2.7						
N50	6.5, -253.5	$3_{03}-2_{02}$	7.8 (0.4)	-1.8 (0.1)	2.9 (0.2)	2.6	0.09 (0.01)	1.21 (0.07)	0.32 (0.02)	3.8	30 (4)	29
		$(3_{21}-2_{20}+3_{22}-2_{21})/2$	0.9 (0.2)	-2.2 (0.3)	3.1 (0.9)	0.3						
N51	18.5, 130.5	$3_{03}-2_{02}$	15.2 (0.5)	-4.0 (0.1)	3.1 (0.1)	4.6	0.12 (0.01)	1.32 (0.05)	0.41 (0.02)	3.2	48 (5)	44
		$(3_{21}-2_{20}+3_{22}-2_{21})/2$	3.5 (0.4)	-4.5 (0.2)	3.1 (0.3)	1.1						
N53	24.5, 178.5	$3_{03}-2_{02}$	14.8 (0.6)	-3.8 (0.1)	5.0 (0.2)	2.8	0.11 (0.01)	2.13 (0.10)	0.40 (0.02)	5.4	45 (5)	45
		$(3_{21}-2_{20}+3_{22}-2_{21})/2$	3.2 (0.4)	-4.6 (0.1)	2.6 (0.4)	1.1						
N54	30.5, 160.5	$3_{03}-2_{02}$	7.2 (0.4)	-4.0 (0.1)	3.1 (0.2)	2.2	0.15 (0.01)	1.32 (0.10)	0.52 (0.05)	2.6	77 (16)	63
		$(3_{21}-2_{20}+3_{22}-2_{21})/2$	2.4 (0.3)	-3.9 (0.3)	4.8 (0.8)	0.5						

Notes. Offsets relative to our reference position for the DR21 filament (see Sect. 2 and Fig. 4). Velocity-integrated intensity, $\int T_{\text{mb}} dv$, local standard of rest velocity, V_{LSR} , full width at half maximum line width (FWHM), and peak temperature (T_{mb}) were obtained from Gaussian fitting using CLASS as part of the GILDAS software package. For the thermal and non-thermal linewidths, σ_{T} and σ_{NT} , the sound velocity c_s , the Mach number M , the kinetic temperature T_{kin} , and the turbulent temperature T_{turb} , see Sects. 3 and 4.3.3. Values in parentheses are uncertainties.

Table 2. Thermal and non-thermal parameters derived from DR21, OMC-1, and N113.

Parameter	DR21 (~0.1 pc)			OMC-1 ^a (~0.06 pc)			N113 ^b (~0.4 pc)		
	Range	Median	Mean	Range	Median	Mean	Range	Median	Mean
H ₂ CO line ratio	0.08–0.42	0.22	0.22 ± 0.01	0.12–0.61	0.21	0.28 ± 0.01	0.10–0.38	0.21	0.22 ± 0.01
T_{kin} /K	23.9–114.5	46.4	48.3 ± 0.5	30–>200	48.5	62.0 ± 2.0	27.6–105.4	48.5	51.4 ± 0.4
σ_{T} /km s ⁻¹	0.08–0.18	0.11	0.11 ± 0.01	0.09–0.27	0.11	0.12 ± 0.01	0.08–0.16	0.11	0.11 ± 0.01
σ_{NT} /km s ⁻¹	0.74–4.40	1.47	1.60 ± 0.02	0.34–2.78	1.64	0.98 ± 0.02	0.93–2.76	1.64	1.69 ± 0.01
c_s /km s ⁻¹	0.29–0.63	0.40	0.41 ± 0.01	0.30–0.97	0.40	0.44 ± 0.01	0.30–0.58	0.40	0.40 ± 0.01
M	1.9–10.3	3.7	4.0 ± 0.1	0.7–4.3	4.2	2.3 ± 0.1	2.3–6.2	4.2	4.2 ± 0.1

Notes. ^(a) Parameters of OMC-1 taken from Tang et al. (2018a). ^(b) Parameters of N113 taken from Tang et al. (2021). The values enclosed in parentheses denote the linear scale of each respective source. The errors shown in Columns 4 and 7 are the standard deviations of the mean.

center clouds (Ao et al. 2013; Ginsburg et al. 2016; Immer et al. 2016).

As detailed in Sect. 1.1, the dust temperature distribution within the DR21 filament has been established through analyzing *Herschel* continuum data observed at 70–500 μm (beam size $\sim 40''$), as reported by both Hennemann et al. (2012) and Cao et al. (2019). The analysis reveals that the dense clumps within our observed region of the DR21 filament exhibit a range of dust temperatures spanning from 15 to 35 K (see Table 3). The typical value, approximately 20 K, is found to be similar to the gas temperature derived from the NH₃ (2,2)/(1,1) line ratios (Mangum et al. 1992; Keown et al. 2019), albeit lower than the results obtained from the H₂CO line ratios (see Sect. 3.4 and Table 1). These findings align with previous observational results in star-forming regions within our galaxy (Tang et al. 2017a, 2018a,b).

In order to facilitate a comparison between the temperatures derived from gas and dust on a larger scale, we have applied

a smoothing technique to our H₂CO data, resulting in a beam size of $\sim 40''$. The peak temperatures obtained from this analysis are approximately 80, 95, 80, and 75 K in the W75S FIR 3, DR21(OH), DR21(OH)S, and DR21 regions, respectively. It is worth noting that these values remain higher than the temperatures measured using NH₃ and dust emission at FIR wavelengths. The structure of dust temperature closely resembles that of the gas temperature obtained through NH₃ and H₂CO observations on a scale of ~ 0.3 pc in the DR21 filament. It is important to note that the emission of dust at FIR wavelengths primarily originates from colder dust components which may not be directly associated with the process of star formation (e.g., Mangum et al. 2013b; Tang et al. 2018a). In comparison to temperature measurements utilizing NH₃ (1,1) and (2,2) and the FIR continuum, the H₂CO lines trace distinctly higher temperatures. This observation confirms that H₂CO may possess sensitivity to

Table 3. Comparison of temperatures and Mach number of different regions.

Region	H ₂ CO K	NH ₃ K	CO K	FIR K	Mach number
W75S	24–95	15–64	41(82/37)	15–25	2.1–7.2
DR21(OH)	26–114	22–64	31(99/29)	15–31	2.2–7.0
DR21	24–87	20–58	36(148/32)	15–>22	1.9–6.7
DR21W1	33–88	35–60	54(118/52)	18–22	2.5–10.3

Notes. Column 2: kinetic temperatures derived from H₂CO line ratios (see Sect. 3.4). Column 3: kinetic temperatures derived from the NH₃ (2,2)/(1,1) line ratios taken from Keown et al. (2019). Column 4: average, warm, and cold components temperatures of low- to high-*J* CO taken from Jakob et al. (2007). Columns 5: far infrared (FIR) dust temperatures taken from Hennemann et al. (2012) and Cao et al. (2019). Columns 6: Mach number derived from H₂CO (see Sect. 3.5).

wards the dense gas that is intimately linked to active star formation.

4.3. Gas Heating

Gas heating in star-forming regions is a multifaceted process that holds paramount significance in the formation and evolution of stars. Acquiring a comprehension of the pivotal role played by gas heating in these regions, measurements of temperature are mandatory to elucidate the underlying mechanisms that drive star formation and shape the evolutionary trajectory of galaxies.

4.3.1. Radiative Heating

Radiative heating plays a pivotal role in the intricate process of star formation, particularly during the initial phases when protostars coalesce within dense molecular clouds. During this period, protostars accrete material and emit substantial amounts of radiation, which interact with and profoundly influence the surrounding ISM. Radiation transfers energy to the ISM through processes such as photoionization, photodissociation, and the generation of photoelectrons. These energy transfer mechanisms result in the heating of the ISM and serve as driving forces behind the subsequent stages of star formation. Previous studies have conducted observations of several molecules, such as NH₃, H₂CO, H₂CS, CH₃CN, CH₃CCH, and CH₃OH, in regions where massive stars are forming (e.g., Lu et al. 2014; Giannetti et al. 2017; Tang et al. 2018a,b, 2021; Gieser et al. 2019, 2021, 2022, 2023; Lin et al. 2022; Wang & Wang 2023). These observations suggest that the dense gas surrounding embedded infrared sources experiences internal radiative heating on scales of $\lesssim 0.1$ – 1.0 pc. As stated in Sects. 3.3 and 3.4, high gas temperatures obtained from H₂CO line ratios associate with dense clumps especially in the W75S FIR 3, DR21(OH), DR21(OH)S, and DR21 regions (see Fig. 4). This indicates that the warm dense gas traced by H₂CO may be influenced by radiation from internally embedded infrared sources. Furthermore, investigations of CO, [CI], [CII], and [OI] emissions in the DR21 region have revealed that the gas experiences significant radiative heating (Lane et al. 1990; Jakob et al. 2007; Ossenkopf et al. 2010).

To investigate the influence of radiation heating on the extended dense gas surrounding massive clumps within the DR21 filament on a scale of ~ 0.1 – 0.3 pc, we conducted a temperature profile analysis of four dense cores situated in the W75S FIR 3, DR21(OH), DR21(OH)S, and DR21 regions (see Fig. 5). These cores, namely N44, N46, N48, and N54, chosen from the respective regions, exhibit distinctly higher kinetic temperatures derived from H₂CO line ratios (see Table 1) than those of the surrounding gas. We note that Fig. 4 shows the spatial distri-

bution of the dense core N38 to the west of N44 and N48 ($\sim 32''$, ~ 0.24 pc), the dense core N42 to the southwest of N46 ($\sim 32''$, ~ 0.24 pc), the dense core N47 to the north of N46 ($\sim 18''$, ~ 0.14 pc), and the dense core N53 to the north of N54 ($\sim 19''$, ~ 0.14 pc). Due to the limited resolution of our observations (beam size $\sim 12''$), we cannot rule out that nearby sources may have influenced the temperature profiles of N44, N46, N48, and N54. To reduce this influence from nearby dense cores, we masked data at the midpoint between selected dense cores and other sources. For the N44 dataset, southern data was masked using a distance threshold exceeding $19''$ along the declination axis. In the case of the N46, both northern and southern data were masked at distances greater than $9''$ and $15''$, respectively. For N48, northern data was masked at a distance exceeding $19''$. Similarly, for N54, northern data was masked using a distance exceeding $10''$. Additionally, for N44 and N48, data corresponding to the dense core N38 (with a radius of $\sim 16''$) was also masked.

In the dense cores N44, N46, and N48, there are significant temperature gradients observed, as depicted in Fig. 5. However, it is worth mentioning that a relatively shallow temperature gradient is detected in dense core N54, which could potentially be attributed to the fact that the dense core is likely in an earlier evolutionary stage (e.g., Motte et al. 2007; Cao et al. 2019), with the embedded protostars or clusters not yet generating sufficient heat to significantly warm the surrounding molecular envelope. As noted above, the dense core N53 is positioned to the north of N54, at a distance of approximately $19''$ (~ 0.14 pc). Previous observations have detected the presence of CH₃OH and H₂O masers in N53 (e.g., Motte et al. 2007), suggesting the occurrence of significant shocks in this area. Additionally, two protostars were identified in the N53/N54 region by Davis et al. (2007) (see Fig. 4). The complex temperature structure observed in the N53/N54 region may be attributed to the impact of outflows and shocks originating from the embedded protostars or clusters within N53 and N54, as well as the radiation emitted by nearby protostars. The temperature profile surrounding these dense clumps can be described by the Stefan-Boltzmann blackbody radiation law, expressed as $T_{\text{kin}} = 0.86 \times (\frac{L}{L_{\odot}})^{1/4} (\frac{R}{\text{pc}})^{-1/2}$ K, where the luminosity L is given in terms of solar luminosity (L_{\odot}) and the distance R is measured in parsecs. By adjusting the emissivity of dust grains to be smaller than the characteristic blackbody temperature wavelength, the radiation law is modified to $T_{\text{kin}} = 2.7 \times (\frac{L}{L_{\odot}})^{1/5} (\frac{R}{\text{pc}})^{-2/5}$ K (Wiseman & Ho 1998; Tang et al. 2018a). The fitted results of the four dense cores are

$$T_{\text{kin}}(\text{N44}) = (268 \pm 30) \times \left(\frac{R}{\text{arcsec}} \right)^{-0.54 \pm 0.04} \text{ K}, \quad (1)$$

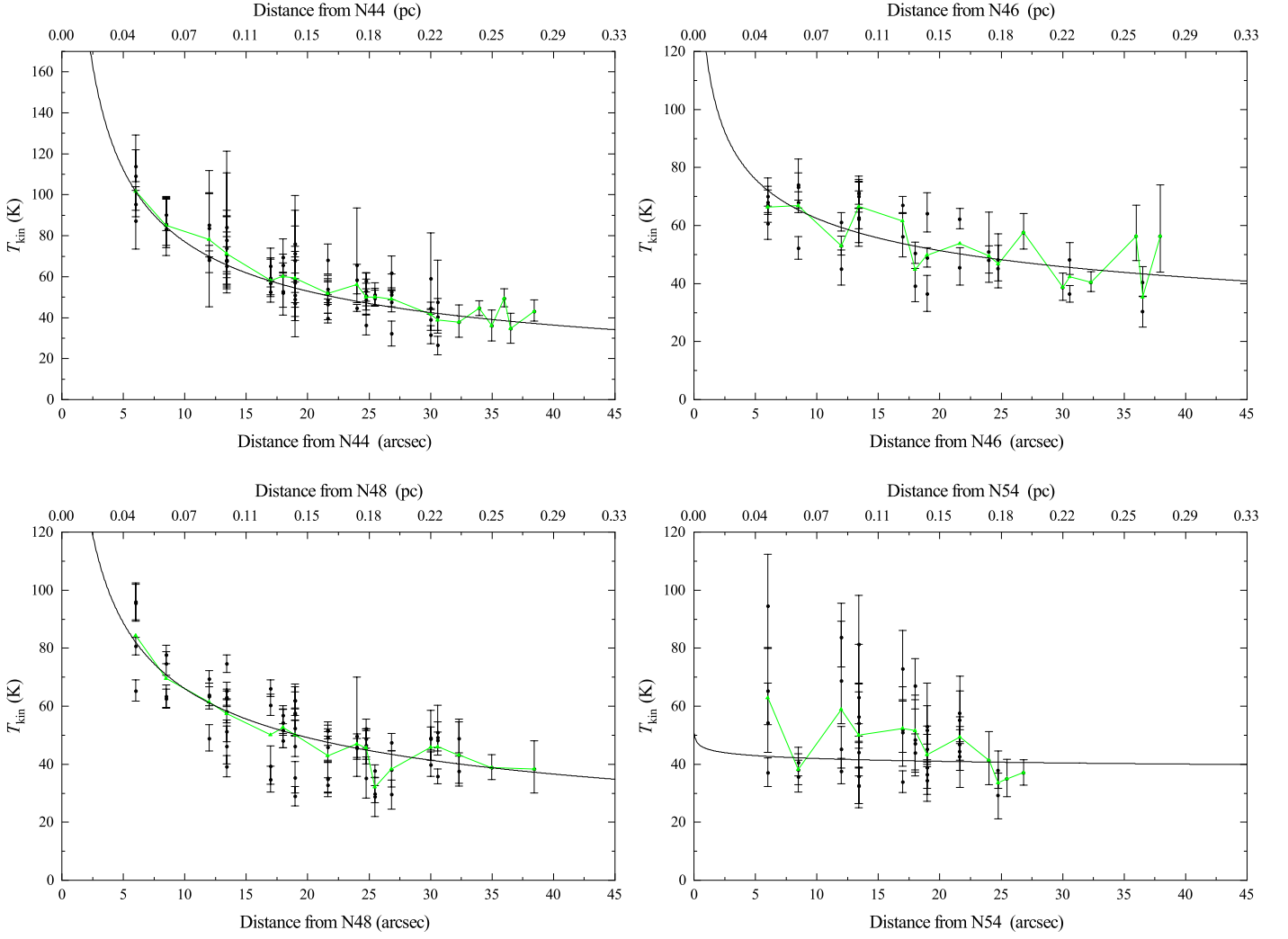


Fig. 5. Gas kinetic temperatures were determined by analyzing the H_2CO (3–2) line ratios from the central regions of the dense cores N44, N46, N48, and N54 (see Table 1), extending towards their respective edges. The format of the regression fits is $T_{\text{kin}}(\text{cores}) = a \times \left(\frac{R}{\text{arcsec}}\right)^b$ K while the fitting method is the Levenberg-Marquardt method without the error of temperature, and the Reduced Chi-Squared values for N44, N46, N48, and N54 are 1.7, 3.3, 5.7, and 1.9, respectively. The average kinetic temperature at each projected distance is represented by green triangles. The green line represents the connection of the each average kinetic temperature, while the fitted results for H_2CO are depicted by black lines.

$$T_{\text{kin}}(\text{N46}) = (120 \pm 16) \times \left(\frac{R}{\text{arcsec}}\right)^{-0.28 \pm 0.05} \text{ K}, \quad (2)$$

$$T_{\text{kin}}(\text{N48}) = (176 \pm 21) \times \left(\frac{R}{\text{arcsec}}\right)^{-0.43 \pm 0.04} \text{ K}, \quad (3)$$

$$T_{\text{kin}}(\text{N54}) = (45 \pm 11) \times \left(\frac{R}{\text{arcsec}}\right)^{-0.03 \pm 0.09} \text{ K}, \quad (4)$$

with power-law indices of -0.54 , -0.28 , -0.43 , and -0.03 for N44, N46, N48, and N54, respectively. With the exception of the dense core N54, the temperature power-law indices obtained from fitting the H_2CO line ratios in our study exhibit consistency with previous observational results with a mean value of about -0.4 . These results align with previous studies that have utilized various molecular tracers such as H_2CO , H_2CS , CH_3CN , and CH_3CCH in the investigation of massive star-forming dense cores (e.g., Gieser et al. 2019, 2021, 2022, 2023; Lin et al. 2022). This indicates that the dense gas heating of the massive cores on a scale of ~ 0.1 – 0.3 pc in the DR21(OH), DR21(OH)S, and

DR21 regions is significantly influenced by internal radiation emitted by associated protostar(s) and/or stellar clusters. The resolution of our observation, ~ 0.1 pc, does not allow for a thorough measurement of the detailed temperature structures within these dense cores. Consequently, a future high-resolution observation is necessary to address this limitation.

4.3.2. Explosive Heating

Explosive heating in molecular clouds refers to the process by which a large amount of energy is rapidly released, leading to a sudden increase in temperature within these clouds. The increased temperature can trigger chemical reactions, influence the stability of the cloud, and even initiate the formation of new stars. It may play a crucial role in the dynamics and evolution of molecular clouds. Understanding the processes and effects of explosive heating is essential for studying the complex interplay between gas dynamics, star formation, and the overall evolution of molecular clouds. Previous observations of H_2CO and H_2CS in the Orion KL region have provided evidence that the dense

gas in this area experiences heating due to shocks induced by a mysterious explosive event that took place several hundred years ago (e.g., Tang et al. 2018a; Li et al. 2020). This event had a significant impact on the energetics of the Orion KL region. Zapata et al. (2013) proposed that the enigmatic northeast–southwest outflow observed in the DR21 region was likely the result of an explosive event that transpired $\sim 10,000$ years ago. This event bears resemblance to the disintegration of a massive stellar system, akin to the occurrence witnessed in Orion KL 500 years ago, albeit with approximately 20 times greater energy output. The accurate location of this explosive event in the DR21 region was identified at $\alpha_{2000} = 20^{\text{h}}39^{\text{m}}01^{\text{s}}.1$ and $\delta_{2000} = 42^{\circ}19'37''.9$ by Zapata et al. (2013). At the location of the DR21 outflow origin, there is no presence of a young star in the radio, submillimeter, or infrared wavelengths. This absence suggests that the potential "source" of the outflow may no longer be situated there, similar to the explosive outflow observed in Orion KL (Zapata et al. 2009, 2013).

The explosive event is observed to occur at the center of an expanding cometary H II region in DR21 (see Fig. 3 in Zapata et al. 2013). As previously mentioned, the heating of dense gas in the DR21 region is greatly influenced by the internal radiation emitted by the associated protostar(s) and/or stellar clusters. In the star formation region of DR21, differentiating between radiation and explosive heating can be challenging but can be done by considering the detailed spatial distribution of T_{kin} . Radiation heating is usually more evenly distributed throughout a star-forming region, as it originates from the young stars themselves. Explosive heating, however, may exhibit localized regions of enhanced heating, corresponding to the locations of energetic events (e.g., Tang et al. 2018a; Li et al. 2020). Previous observations suggest that H₂CO could serve as a promising indicator for detecting outflows or shocks (e.g., Tang et al. 2017b; Lu et al. 2021; Izumi et al. 2023). As stated in Sect. 3.5, the DR21 region exhibits substantial non-thermal linewidths ($\sigma_{\text{NT}} \sim 2.3 \text{ km s}^{-1}$) and Mach numbers ($M \sim 4.5$), as depicted in Fig. 4. Their correlation suggests that the dense gas, which is traced by H₂CO, may be influenced by the shocks resulting from explosive flows and/or expanding H II regions. To investigate the impact of the explosive event on the heating of dense gas in the DR21 region, we conducted an analysis of the temperature structure within the dense core N46 (see Figs. 4 and 5) which is located at the putative position of the supposed explosive event (Zapata et al. 2013). The analysis of H₂CO data reveals that the gas temperature within the dense core N46 of the DR21 region is measured to be 77 K. This temperature is lower than that observed in the dense cores N44 and N48 of the DR21(OH) and DR21(OH)S regions. Furthermore, the temperature gradient observed in the DR21 region is flatter when compared to the temperature gradients observed in the DR21(OH) and DR21(OH)S regions (see Fig. 5). As previously noted, the dense gas may exhibit localized regions of increased heat when subjected to heating by an explosive event. However, a relatively uniform temperature gradient in the DR21 region is inconsistent with this pattern of explosive heating. As delineated in the preceding section, the temperature profile derived from the dense core N46 aligns with the results anticipated from radiation heating. The heating of the dense gas in the DR21 region may be partly attributed to the shocks generated by an explosive event that occurred a long time ago. However, our temperature measurements with H₂CO do not provide direct evidence to support the hypothesis that the dense gas is heated by shocks resulting from a past explosive event on a scale of ~ 0.1 pc in the DR21 region.

Zapata et al. (2013) proposed that the DR21 north-east–southwest outflow was likely generated by a powerful explosion occurring $\sim 10,000$ years ago. However, the genesis of the DR21 outflow remains a subject of ongoing investigation (e.g., Skretas et al. 2023). Previous observations suggest that the DR21W1 region is correlated with the western DR21 flow (e.g., Jaffe et al. 1989; Lane et al. 1990; Wilson & Mauersberger 1990; Garden et al. 1991a,b; Garden & Carlstrom 1992; Davis et al. 2007). It appears that a high temperature (~ 84 K) associates with the dense core N34 in the DR21W1 region (see Fig. 4). A flat temperature structure, analogous to that of the DR21 region, was detected in the DR21W1 region. The highest non-thermal linewidths ($\sigma_{\text{NT}} \sim 4.4 \text{ km s}^{-1}$) and Mach numbers ($M \sim 10$) of the entire DR21 filament are found in the northeastern and southern region of DR21W1 (see Fig. 4). These confirm that the dense gas in the DR21W1 region is strongly influenced by shocks which may be caused by explosive flows. In the DR21W1 region, Cao et al. (2019) discovered an infrared-quiet massive dense core with a luminosity of $\sim 350 L_{\odot}$. The absence of strong $8 \mu\text{m}$ emission in this region (refer to Fig. 1 in Kumar et al. 2007) suggests that the dense core is in an early evolutionary stage. In the study conducted, the gas temperature in the DR21W1 region, which is influenced by young stellar objects (YSOs), was determined using the modified Stefan-Boltzmann blackbody radiation law (refer to Sect. 4.3.1). It was assumed that the embedded YSOs (or YSO candidates) serve as the primary sources of energy in the DR21W1 region, with a luminosity of $\sim 350 L_{\odot}$ as reported by Cao et al. (2019). The derived gas temperature from the modified Stefan-Boltzmann blackbody radiation law was found to be ~ 22 K at radii of 0.1 pc, which is significantly lower than the typical temperature of 70–80 K obtained from the measurements of H₂CO line ratios. This indicates that the radiation heating from internal embedded YSOs (or YSO candidates) only affects the local region. The high temperatures of dense gas in the DR21W1 region should be dominated by the shocks from the western DR21 flow. Our measurements of H₂CO towards the DR21W1 region provide compelling evidence that the dense gas in this area is heated by shocks which may arise from explosive flows.

4.3.3. Turbulent Heating

Turbulence is a prevalent phenomenon observed in various phases of the interstellar medium (Mac Low & Klessen 2004; Elmegreen & Scalo 2004; Scalo & Elmegreen 2004; Sokolov et al. 2018; Wang & Wang 2023; Wang et al. 2023). Recent observations conducted on Galactic Central Molecular Zone clouds using H₂CO (3–2 and 4–3) indicate that the warm dense gas is primarily heated by turbulence occurring on a scale of ~ 1 pc (Ao et al. 2013; Ginsburg et al. 2016; Immer et al. 2016). In Galactic massive star-forming regions, it appears that molecular gas heated by turbulence is commonly encountered (Tang et al. 2018a,b, 2021). Notably, multiple observations utilizing molecular tracers, including H₂CO, NH₃, and CH₃CCH, in star formation regions, indicate a significant correlation between linewidth and gas kinetic temperature (Wouterloot et al. 1988; Molinari et al. 1996; Jijina et al. 1999; Wu et al. 2006; Urquhart et al. 2011, 2015; Wienen et al. 2012; Lu et al. 2014; Giannetti et al. 2017; Tang et al. 2017a, 2018a,b, 2021). As a result, higher temperatures inferred from various tracers align with elevated turbulence levels.

We investigate the potential relationship between turbulence and temperature on a scale of ~ 0.1 pc within the DR21 filament. To assess turbulence, we utilize the non-thermal linewidth

(σ_{NT}) of H_2CO , which serves as a reliable indicator. Additionally, we determine the gas kinetic temperature using the H_2CO line ratio. Specifically, we focus on positions near dense regions that exhibit strong non-thermal motions ($\mathcal{M} \gtrsim 3.0$). As stated in Sect 3.5, the dense gas in locations characterized by higher Mach numbers ($\mathcal{M} \gtrsim 3.0$) is significantly impacted by non-thermal motions. Therefore, for our analysis, we specifically choose positions in close proximity to W75S FIR 3, W75S FIR 2, DR21(OH)S, DR21, and DR21W1. In Fig. 6, we present the correlation between the non-thermal linewidth and gas kinetic temperature for both the H_2CO $3_{03-2_{02}}$ line and the combined H_2CO $3_{22-2_{21}}$ and $3_{21-2_{20}}$ lines. A power law relationship is fitted, with $T_{\text{kin}} \propto \sigma_{\text{NT}}^{0.42 \pm 0.04}$ for H_2CO $3_{03-2_{02}}$ and $T_{\text{kin}} \propto \sigma_{\text{NT}}^{0.41 \pm 0.03}$ for the combined H_2CO $3_{22-2_{21}}$ and $3_{21-2_{20}}$ lines. The correlation coefficients, R , are determined to be 0.45 and 0.55, respectively. These results suggest that the elevated temperature observed in regions of strong non-thermal motion within the DR21 filament, as indicated by H_2CO , can be attributed to turbulence occurring at a scale of ~ 0.1 pc, which aligns with previous observational studies conducted on massive star-forming clumps (ATLASGAL sample, Tang et al. 2018b) and the Orion molecular cloud 1 (OMC-1, Tang et al. 2018a), where similar temperature variations were observed on a scale ranging from approximately 0.06 to 2 pc. One should note that this agreement pertains solely to the intercept and not the power law index (see Fig. 6). The power law index fitted in the DR21 filament is approximately 0.41-0.42, which is lower than the previous observational results ($T_{\text{kin}} \propto \sigma_{\text{NT}}^{0.76-1.26}$) in the ATLASGAL sample and OMC-1 (Tang et al. 2018a,b). As previously mentioned, the dense gas in the DR21 filament is also influenced by various factors, such as outflows, shocks, and/or radiation from regions of massive star formation in W75S, DR21(OH), and DR21. The variation in the power law index could be attributed to the disparity in the contribution fractions of gas heating mechanisms to the gas temperature between the DR21 filament and the ATLASGAL sample, as well as OMC-1.

Assuming that the dominant factor heating the gas is turbulence, we employ the methodology outlined by Tang et al. (2018a) in their Equation (2) to compute the gas kinetic temperature, denoted as T_{turb} , resulting from turbulence in the DR21 filament. Our calculations are based on the following assumptions: a gas density of $n(\text{H}_2) = 10^5 \text{ cm}^{-3}$, a typical velocity gradient of $1 \text{ km s}^{-1} \text{ pc}^{-1}$, the non-thermal linewidth values of H_2CO provided in Table 1, a cloud size of ~ 1 pc, and a dust temperature equal to the gas temperature derived from H_2CO . The computed T_{turb} values are presented in Table 1, revealing a notable correlation between the derived T_{turb} value and the kinetic temperature obtained from the H_2CO line ratio. These results suggest that turbulence plays a significant role in determining the dense gas kinetic temperature on a scale of ~ 0.1 pc in the DR21 filament.

4.4. Comparison with the OMC-1 and N113

The Orion molecular cloud 1 is a well-known target for studying the physical and chemical properties of molecular clouds and their role in star formation. Its complex gas heating has been revealed by observations made with the APEX 12 m telescope over a region of size $\sim 1.1 \times 1.7 \text{ pc}^2$, where the same H_2CO (3–2) lines were mapped on a scale of ~ 0.06 pc (Tang et al. 2018a). The complex gas heating in the OMC-1 is likely due to multiple processes including star formation activity, radiation, and turbulence. The N113 region, which is located in the Large Magellanic Cloud, is a well-studied site for massive star formation and shows strong molecular line emission (e.g., Tang et al. 2017a,

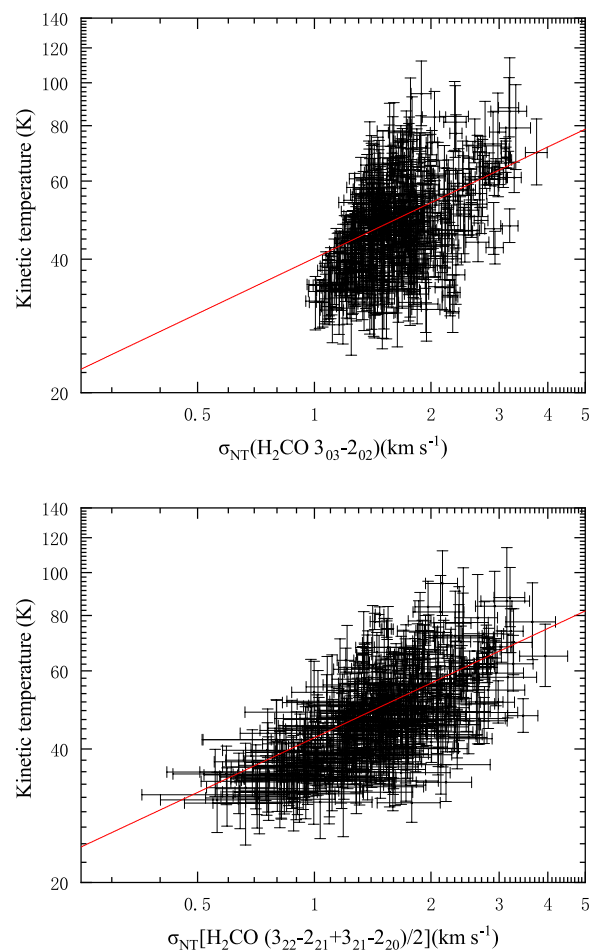


Fig. 6. The relationship between the non-thermal linewidth (σ_{NT}) and gas kinetic temperature, as determined from the H_2CO line ratio, is examined in those parts of the DR21 filament, which are characterized by a Mach number $\mathcal{M} \gtrsim 3.0$ (see Sect. 4.3.3). A linear fit is applied to the H_2CO $3_{03-2_{02}}$ and the combined H_2CO $3_{22-2_{21}}$ and $3_{21-2_{20}}$ lines, yielding the following results: $\log T_{\text{kin}} = (0.42 \pm 0.04) \times \log \sigma_{\text{NT}} + (1.60 \pm 0.01)$ and $\log T_{\text{kin}} = (0.41 \pm 0.03) \times \log \sigma_{\text{NT}} + (1.63 \pm 0.01)$, respectively. In this fitting, the linear fit was performed on the unweighted data using the least squares method. The Pearson correlation coefficients, R , for these fits (red lines) are 0.45 and 0.55, respectively.

2021; Gong et al. 2023a). The complex gas heating in N113 was also studied using an ALMA survey over a relatively large area of N113 ($\sim 2.4 \times 6.1 \text{ pc}^2$), where the transitions of the same H_2CO (3–2) lines were detected on a linear scale of ~ 0.4 pc (Tang et al. 2018b). The gas heating process in N113 appears to be as intricate as that of its counterpart in OMC-1.

As discussed above, our observations in the DR21 filament ($\sim 1.4 \times 4.4 \text{ pc}^2$) on a scale of ~ 0.1 pc also indicate the presence of similar gas heating mechanisms as in OMC-1 and N113. In addition, we compare the detailed physical parameters of dense gas, H_2CO line ratio, T_{kin} , σ_{T} , σ_{NT} , c_{s} , and \mathcal{M} , derived from H_2CO (3–2) lines in the DR21 filament, OMC-1, and N113 in Table 2. The median values of these physical parameters in the dense gas within the DR21 filament appear to be nearly identical to the results obtained in OMC-1 and N113 on a scale of ~ 0.1 – 0.4 pc (see Table 2). It should be noted that the mean values of non-thermal linewidth and Mach number in OMC-1 are marginally lower than those observed in DR21 and N113. This discrepancy may be attributed to the superior resolution

of OMC-1 (beam size ~ 0.06 pc) and/or the inherent turbulence fluctuations across various molecular clouds. These similarities in physical parameters suggest that the processes governing the dynamics and thermodynamics of the dense gas traced by H_2CO in different star formation regions may share common underlying principles, despite variations in specific environmental conditions. The dense gas in star formation regions is influenced by similar environmental factors, such as gravitational collapse, turbulent motions, and thermal processes, which contribute to the consistency in these parameters across various regions and evolutionary stages. The physical conditions in star-forming regions appear to be shaped by similar mechanisms, leading to the convergence of these parameters. This can include processes such as supersonic turbulence, thermal pressure, and the interaction between magnetic fields and turbulent motions, all of which contribute to the observed similarities in the physical parameters.

5. Summary

The kinetic temperature structure of the massive filament DR21 in the Cygnus X molecular cloud complex has been mapped using the H_2CO 218 GHz line triplet observed with the IRAM 30 m telescope. The main results are the following:

1. The H_2CO $3_{03}-2_{02}$ emission exhibits an extensive distribution and provides a clear measurement of the dense ridge structure of the DR21 filament.
2. By employing the RADEX non-LTE model, we have determined the gas temperature through the modeling of the measured H_2CO $0.5 \times [(3_{22}-2_{21} + 3_{21}-2_{20})/3_{03}-2_{02}]$ line ratios. The derived gas kinetic temperatures exhibit a range, varying from 24 to 114 K, with an average of 48.3 ± 0.5 K at a spatial density of 10^5 cm^{-3} . In comparison to temperature measurements utilizing NH_3 (1,1)/(2,2) and FIR wavelengths, the H_2CO lines trace distinctly higher temperatures.
3. The dense gas, traced by H_2CO , exhibiting kinetic temperatures in excess of 50 K appears to be correlated with the dense clumps found in various regions, namely W75S FIR 3, DR21(OH), DR21(OH)W, DR21(OH)S, DR21, and DR21W1. On the other hand, the outskirts of the DR21 filament show lower temperature distributions ($T_{\text{kin}} < 50$ K).
4. Four dense cores, N44, N46, N48, and N54, located in the DR21(OH), DR21, DR21(OH)S, and W75S FIR 3 regions, respectively, exhibit temperature gradients on a scale of approximately 0.1–0.3 pc. This suggests that the warm dense gas traced by H_2CO is influenced by internal star formation activity. Unlike the dense core N54, the temperature profiles of these dense cores could be fitted with power-law indices ranging from -0.3 to -0.5 , with a mean value of ~ -0.4 , indicating that the warm dense gas probed by H_2CO is heated by radiation emitted from internally embedded protostar(s) and/or stellar clusters.
5. In the DR21 region, our temperature measurements towards the dense core N46, located at the putative position of a supposed major explosive event, provide no direct evidence supporting this notion on a scale of ~ 0.1 pc. Nevertheless, we find compelling evidence that the dense gas in the DR21W1 region is indeed heated by shocks originating from the western DR21 flow.
6. The non-thermal linewidths of H_2CO exhibit a correlation with the gas kinetic temperatures within the DR21 filament. This suggests that higher temperatures, as traced by H_2CO , are associated with turbulence on a scale of ~ 0.1 pc.
7. The physical parameters of the dense gas, as determined from H_2CO lines in the DR21 filament, exhibit a striking similarity to the results obtained in OMC-1 and N113 on a scale of approximately 0.1–0.4 pc. This may imply that the mechanisms governing the dynamics and thermodynamics of dense gas traced by H_2CO in diverse star formation regions may be governed by common underlying principles, despite variations in specific environmental conditions.

Acknowledgements. We thank the staff of the IRAM telescope for their assistance in observations. This work acknowledges the support of the National Key R&D Program of China under grant No. 2023YFA1608002, the Chinese Academy of Sciences (CAS) “Light of West China” Program under grant No. xbgz-zdsys-202212, the Tianshan Talent Program of Xinjiang Uygur Autonomous Region under grant No. 2022TSYCLJ0005, and the Natural Science Foundation of Xinjiang Uygur Autonomous Region under grant No. 2022D01E06. It was also partially supported by the National Key R&D Program of China under grant No. 2022YFA1603103, the CAS “Light of West China” Program under grant No. 2020-XBQNXZ-017, the National Natural Science Foundation of China under grant Nos. 12173075 and 12373029, and the Youth Innovation Promotion Association CAS. T. Liu, K. Wang, X. P. Chen, and J. W. Wu acknowledge support by the Tianchi Talent Program of Xinjiang Uygur Autonomous Region. C. Henkel acknowledges support by the Chinese Academy of Sciences President’s International Fellowship Initiative under grant Nos. 2023VMA0031 and 2025PVA0048. This research has used NASA’s Astrophysical Data System (ADS).

References

- Ao, Y., Henkel, C., Menten, K. M., et al. 2013, *A&A*, 550, A135
- Batrla, W. & Menten, K. M. 1988, *ApJ*, 329, L117
- Battersby, C., Bally, J., Dunham, M., et al. 2014, *ApJ*, 786, 116
- Beerer, I. M., Koenig, X. P., Hora, J. L., et al. 2010, *ApJ*, 720, 679
- Bonne, L., Bontemps, S., Schneider, N., et al. 2023, *ApJ*, 951, 39
- Brinkmann, N., Wyrowski, F., Kauffmann, J., et al. 2020, *A&A*, 636, A39
- Cao, Y., Qiu, K., Zhang, Q., & Li, G.-X. 2022, *ApJ*, 927, 106
- Cao, Y., Qiu, K., Zhang, Q., et al. 2019, *ApJS*, 241, 1
- Caselli, P., Hasegawa, T. I., & Herbst, E. 1993, *ApJ*, 408, 548
- Chandler, C. J., Gear, W. K., & Chini, R. 1993, *MNRAS*, 260, 337
- Ching, T.-C., Qiu, K., Li, D., et al. 2022, *ApJ*, 941, 122
- Csengeri, T., Bontemps, S., Schneider, N., Motte, F., & Dib, S. 2011, *A&A*, 527, A135
- Cyganowski, C. J., Reid, M. J., Fish, V. L., & Ho, P. T. P. 2003, *ApJ*, 596, 344
- Davis, C. J., Kumar, M. S. N., Sandell, G., et al. 2007, *MNRAS*, 374, 29
- Dewangan, L. K., Ojha, D. K., Luna, A., et al. 2016, *ApJ*, 819, 66
- Dobashi, K., Shimoikura, T., Katakura, S., Nakamura, F., & Shimajiri, Y. 2019, *PASJ*, 71, S12
- Downes, D., Wilson, T. L., Bieging, J., & Wink, J. 1980, *A&AS*, 40, 379
- Dunham, M. K., Rosolowsky, E., Evans, Neal J., I., Cyganowski, C., & Urquhart, J. S. 2011, *ApJ*, 741, 110
- Dunham, M. K., Rosolowsky, E., Evans, Neal J., I., et al. 2010, *ApJ*, 717, 1157
- Elmegreen, B. G. & Scalzo, J. 2004, *ARA&A*, 42, 211
- Garden, R. P. & Carlstrom, J. E. 1992, *ApJ*, 392, 602
- Garden, R. P., Geballe, T. R., Gatley, I., & Nadeau, D. 1991a, *ApJ*, 366, 474
- Garden, R. P., Hayashi, M., Gatley, I., Hasegawa, T., & Kaifu, N. 1991b, *ApJ*, 374, 540
- Genzel, R. & Downes, D. 1977, *A&AS*, 30, 145
- Gerner, T., Beuther, H., Semenov, D., et al. 2014, *A&A*, 563, A97
- Giannetti, A., Brand, J., Sánchez-Monge, Á., et al. 2013, *A&A*, 556, A16
- Giannetti, A., Leurini, S., Wyrowski, F., et al. 2017, *A&A*, 603, A33
- Gieser, C., Beuther, H., Semenov, D., et al. 2023, *A&A*, 674, A160
- Gieser, C., Beuther, H., Semenov, D., et al. 2021, *A&A*, 648, A66
- Gieser, C., Beuther, H., Semenov, D., et al. 2022, *A&A*, 657, A3
- Gieser, C., Semenov, D., Beuther, H., et al. 2019, *A&A*, 631, A142
- Ginsburg, A., Darling, J., Battersby, C., Zeiger, B., & Bally, J. 2011, *ApJ*, 736, 149
- Ginsburg, A., Henkel, C., Ao, Y., et al. 2016, *A&A*, 586, A50
- Goldsmith, P. F. 2001, *ApJ*, 557, 736
- Gong, Y., Henkel, C., Menten, K. M., et al. 2023a, *A&A*, 679, L6
- Gong, Y., Henkel, C., Spezzano, S., et al. 2015a, *A&A*, 574, A56
- Gong, Y., Henkel, C., Thorwirth, S., et al. 2015b, *A&A*, 581, A48
- Gong, Y., Ortiz-León, G. N., Rugel, M. R., et al. 2023b, *A&A*, 678, A130
- Guo, W. H., Esimbek, J., Di Tang, X., et al. 2016, *Ap&SS*, 361, 264
- Harris, S. 1973, *MNRAS*, 162, 5P
- Harvey, P. M., Joy, M., Lester, D. F., & Wilking, B. A. 1986, *ApJ*, 300, 737

- Harvey-Smith, L., Soria-Ruiz, R., Duarte-Cabral, A., & Cohen, R. J. 2008, *MNRAS*, 384, 719
- Henkel, C., Braatz, J. A., Menten, K. M., & Ott, J. 2008, *A&A*, 485, 451
- Henkel, C., Walmsley, C. M., & Wilson, T. L. 1980, *A&A*, 82, 41
- Henkel, C., Wilson, T. L., & Mauersberger, R. 1987, *A&A*, 182, 137
- Henkel, C., Wilson, T. L., Walmsley, C. M., & Pauls, T. 1983, *A&A*, 127, 388
- Hennemann, M., Motte, F., Schneider, N., et al. 2012, *A&A*, 543, L3
- Ho, P. T. P. & Townes, C. H. 1983, *ARA&A*, 21, 239
- Hurt, R. L., Barsony, M., & Wootten, A. 1996, *ApJ*, 456, 686
- Immer, K., Kauffmann, J., Pillai, T., Ginsburg, A., & Menten, K. M. 2016, *A&A*, 595, A94
- Izumi, N., Sanhueza, P., Koch, P. M., et al. 2023, arXiv e-prints, arXiv:2312.03935
- Jaffe, D. T., Genzel, R., Harris, A. I., et al. 1989, *ApJ*, 344, 265
- Jakob, H., Kramer, C., Simon, R., et al. 2007, *A&A*, 461, 999
- Jijina, J., Myers, P. C., & Adams, F. C. 1999, *ApJS*, 125, 161
- Johnston, K. G., Beuther, H., Linz, H., et al. 2014, *A&A*, 568, A56
- Johnstone, D., Boonman, A. M. S., & van Dishoeck, E. F. 2003, *A&A*, 412, 157
- Kahle, K. A., Hernández-Gómez, A., Wyrowski, F., & Menten, K. M. 2023, *A&A*, 673, A143
- Kennicutt, Robert C., J. 1998a, *ARA&A*, 36, 189
- Kennicutt, Robert C., J. 1998b, *ApJ*, 498, 541
- Keown, J., Di Francesco, J., Rosolowsky, E., et al. 2019, *ApJ*, 884, 4
- Klessen, R. S., Spaans, M., & Jappsen, A.-K. 2007, *MNRAS*, 374, L29
- Kogan, L. & Slysh, V. 1998, *ApJ*, 497, 800
- Krieger, N., Ott, J., Beuther, H., et al. 2017, *ApJ*, 850, 77
- Kumar, M. S. N., Davis, C. J., Grave, J. M. C., Ferreira, B., & Froebrich, D. 2007, *MNRAS*, 374, 54
- Lane, A. P., Haas, M. R., Hollenbach, D. J., & Erickson, E. F. 1990, *ApJ*, 361, 132
- Li, D., Tang, X., Henkel, C., et al. 2020, *ApJ*, 901, 62
- Lin, Y., Wyrowski, F., Liu, H. B., et al. 2022, *A&A*, 658, A128
- Lindberg, J. E., Jørgensen, J. K., Watanabe, Y., et al. 2015, *A&A*, 584, A28
- Liu, H.-L., Sanhueza, P., Liu, T., et al. 2020, *ApJ*, 901, 31
- Lu, X., Li, S., Ginsburg, A., et al. 2021, *ApJ*, 909, 177
- Lu, X., Zhang, Q., Kauffmann, J., et al. 2017, *ApJ*, 839, 1
- Lu, X., Zhang, Q., Liu, H. B., Wang, J., & Gu, Q. 2014, *ApJ*, 790, 84
- Mac Low, M.-M. & Klessen, R. S. 2004, *Reviews of Modern Physics*, 76, 125
- Mangum, J. G., Darling, J., Henkel, C., & Menten, K. M. 2013a, *ApJ*, 766, 108
- Mangum, J. G., Darling, J., Henkel, C., et al. 2013b, *ApJ*, 779, 33
- Mangum, J. G., Darling, J., Menten, K. M., & Henkel, C. 2008, *ApJ*, 673, 832
- Mangum, J. G., Ginsburg, A. G., Henkel, C., et al. 2019, *ApJ*, 871, 170
- Mangum, J. G. & Wootten, A. 1993, *ApJS*, 89, 123
- Mangum, J. G., Wootten, A., & Barsony, M. 1999, *ApJ*, 526, 845
- Mangum, J. G., Wootten, A., Loren, R. B., & Wadiak, E. J. 1990, *ApJ*, 348, 542
- Mangum, J. G., Wootten, A., & Mundy, L. G. 1992, *ApJ*, 388, 467
- Mangum, J. G., Wootten, A., & Plambeck, R. L. 1993, *ApJ*, 409, 282
- Marston, A. P., Reach, W. T., Noriega-Crespo, A., et al. 2004, *ApJS*, 154, 333
- Mazumdar, P., Tram, L. N., Wyrowski, F., Menten, K. M., & Tang, X. 2022, *A&A*, 668, A180
- Merello, M., Molinari, S., Rygl, K. L. J., et al. 2019, *MNRAS*, 483, 5355
- Molinari, S., Brand, J., Cesaroni, R., & Palla, F. 1996, *A&A*, 308, 573
- Motte, F., Bontemps, S., Schilke, P., et al. 2007, *A&A*, 476, 1243
- Mühle, S., Seaquist, E. R., & Henkel, C. 2007, *ApJ*, 671, 1579
- Nagy, Z., van der Tak, F. F. S., Fuller, G. A., Spaans, M., & Plume, R. 2012, *A&A*, 542, A6
- Norris, R. P., Booth, R. S., Diamond, P. J., & Porter, N. D. 1982, *MNRAS*, 201, 191
- Ossenkopf, V., Röllig, M., Simon, R., et al. 2010, *A&A*, 518, L79
- Ott, J., Weiß, A., Staveley-Smith, L., Henkel, C., & Meier, D. S. 2014, *ApJ*, 785, 55
- Pan, L. & Padoan, P. 2009, *ApJ*, 692, 594
- Papadopoulos, P. P., Thi, W.-F., Miniati, F., & Viti, S. 2011, *MNRAS*, 414, 1705
- Paumard, T., Genzel, R., Martins, F., et al. 2006, *ApJ*, 643, 1011
- Qin, S.-L., Zhao, J.-H., Moran, J. M., et al. 2008, *ApJ*, 677, 353
- Reipurth, B. & Schneider, N. 2008, in *Handbook of Star Forming Regions, Volume I*, ed. B. Reipurth, Vol. 4, 36
- Russell, A. P. G., Bally, J., Padman, R., & Hills, R. E. 1992, *ApJ*, 387, 219
- Rygl, K. L. J., Brunthaler, A., Sanna, A., et al. 2012, *A&A*, 539, A79
- Scalo, J. & Elmegreen, B. G. 2004, *ARA&A*, 42, 275
- Schneider, N., Bontemps, S., Motte, F., et al. 2016, *A&A*, 587, A74
- Schneider, N., Bontemps, S., Simon, R., et al. 2006, *A&A*, 458, 855
- Schneider, N., Csengeri, T., Bontemps, S., et al. 2010, *A&A*, 520, A49
- Schuster, K. F., Boucher, C., Brunswig, W., et al. 2004, *A&A*, 423, 1171
- Shirley, Y. L. 2015, *PASP*, 127, 299
- Skretas, I. M., Karska, A., Wyrowski, F., et al. 2023, *A&A*, 679, A66
- Sokolov, V., Wang, K., Pineda, J. E., et al. 2018, *A&A*, 611, L3
- Tang, X. D., Esimbek, J., Zhou, J. J., et al. 2013, *A&A*, 551, A28
- Tang, X.-D., Esimbek, J., Zhou, J.-J., Wu, G., & Okoh, D. 2014, *Research in Astronomy and Astrophysics*, 14, 959
- Tang, X. D., Henkel, C., Chen, C. H. R., et al. 2017a, *A&A*, 600, A16
- Tang, X. D., Henkel, C., Menten, K. M., et al. 2021, *A&A*, 655, A12
- Tang, X. D., Henkel, C., Menten, K. M., et al. 2019, *A&A*, 629, A6
- Tang, X. D., Henkel, C., Menten, K. M., et al. 2018a, *A&A*, 609, A16
- Tang, X. D., Henkel, C., Menten, K. M., et al. 2017b, *A&A*, 598, A30
- Tang, X. D., Henkel, C., Wyrowski, F., et al. 2018b, *A&A*, 611, A6
- Tursun, K., Esimbek, J., Henkel, C., et al. 2020, *A&A*, 643, A178
- Urquhart, J. S., Figura, C. C., Moore, T. J. T., et al. 2015, *MNRAS*, 452, 4029
- Urquhart, J. S., Morgan, L. K., Figura, C. C., et al. 2011, *MNRAS*, 418, 1689
- Vallée, J. P. & Fiege, J. D. 2006, *ApJ*, 636, 332
- van der Tak, F. F. S., Black, J. H., Schöier, F. L., Jansen, D. J., & van Dishoeck, E. F. 2007, *A&A*, 468, 627
- Wang, C. & Wang, K. 2023, *A&A*, 674, A46
- Wang, C., Wang, K., Xu, F.-W., et al. 2023, arXiv e-prints, arXiv:2310.17970
- Wang, K., Zhang, Q., Wu, Y., Li, H.-b., & Zhang, H. 2012, *ApJ*, 745, L30
- Watanabe, T. & Mitchell, G. F. 2008, *AJ*, 136, 1947
- Wienen, M., Wyrowski, F., Schuller, F., et al. 2012, *A&A*, 544, A146
- Wiesenfeld, L. & Faure, A. 2013, *MNRAS*, 432, 2573
- Wilson, T. L. & Mauersberger, R. 1990, *A&A*, 239, 305
- Wiseman, J. J. & Ho, P. T. P. 1998, *ApJ*, 502, 676
- Wouterloot, J. G. A., Walmsley, C. M., & Henkel, C. 1988, *A&A*, 203, 367
- Wu, Y., Zhang, Q., Yu, W., et al. 2006, *A&A*, 450, 607
- Yan, Y. T., Zhang, J. S., Henkel, C., et al. 2019, *ApJ*, 877, 154
- Zapata, L. A., Loinard, L., Su, Y. N., et al. 2012, *ApJ*, 744, 86
- Zapata, L. A., Schmid-Burgk, J., Ho, P. T. P., Rodríguez, L. F., & Menten, K. M. 2009, *ApJ*, 704, L45
- Zapata, L. A., Schmid-Burgk, J., Pérez-Goytia, N., et al. 2013, *ApJ*, 765, L29
- Zhang, X., Qiu, K., Zhang, Q., et al. 2024, *A&A*, 684, A142
- Zhang, Z.-Y., Romano, D., Ivison, R. J., Papadopoulos, P. P., & Matteucci, F. 2018, *Nature*, 558, 260

Appendix A: H₂CO Velocity Channel Maps

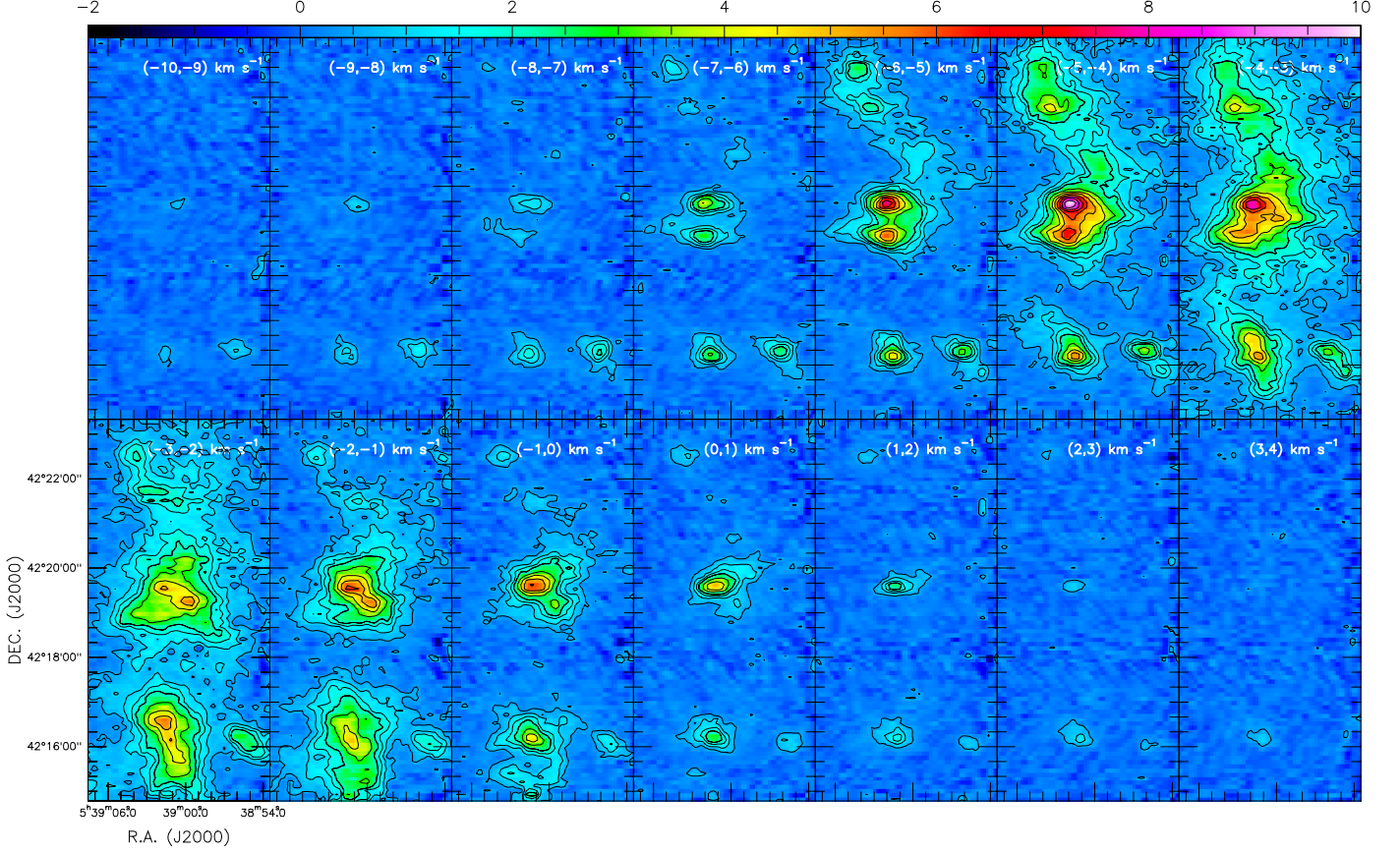


Fig. A.1. Channel maps of the H₂CO (3₀₃–2₀₂) transition. The contour levels are running from 0.5 to 2.0 K in steps of 0.5 K and from 2 to 10 K in steps of 1 K (T_{mb} scale; color bar in units of K).

Appendix B: The LTE and Non-LTE Models for H₂CO

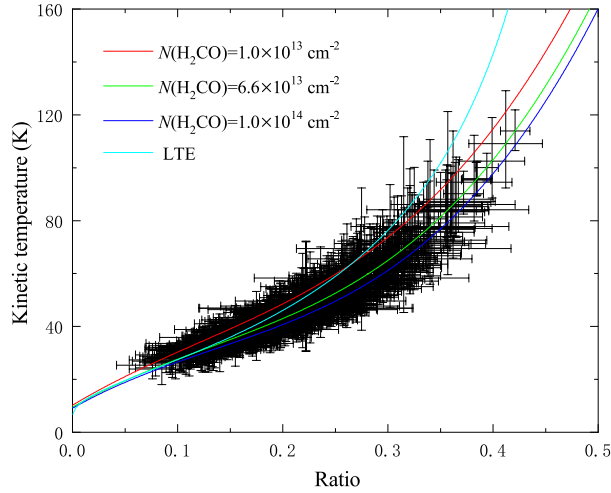


Fig. B.1. RADEX non-LTE modeling of the relation between the kinetic temperature and the average ratio of H₂CO 3₂₂–2₂₁/3₀₃–2₀₂ and 3₂₁–2₂₀/3₀₃–2₀₂ with an assumed density of $n(\text{H}_2)=10^5 \text{ cm}^{-3}$ and column densities $N(\text{para-H}_2\text{CO})=1.0 \times 10^{13}$, 6.6×10^{13} and $1.0 \times 10^{14} \text{ cm}^{-2}$ (red, green, and blue), and the LTE (cyan), and an averaged linewidth of 3.8 km s^{-1} . The LTE kinetic temperature (T_{LTE}) is determined using the methodology described in Mangum & Wootten (1993) and Tang et al. (2017b). T_{LTE} is calculated as $T_{\text{LTE}} = \frac{47.1}{\ln(0.556/\text{Ratio})}$ K, where Ratio represents the average ratio of H₂CO 3₂₂–2₂₁/3₀₃–2₀₂ and 3₂₁–2₂₀/3₀₃–2₀₂. The black points are derived from our observed H₂CO line ratios from the DR21 filament for a column density $N(\text{para-H}_2\text{CO}) = 6.6 \times 10^{13} \text{ cm}^{-2}$. The temperature uncertainties are obtained from observed H₂CO line ratio errors.